AFRL-AFOSR-UK-TR-2022-0019

Improvement of Physical Modeling for Vortex-Dominated Flows

Krumbein, Andreas
DEUTSCHES ZENTRUM FUR LUFT- UND RAUMFAHRT E.V.
LINDER HOHE
KOLN, NORDRHEIN-WESTFALEN, 51147
DEU

01/24/2022
Final Technical Report

Air Force Research Laboratory
Air Force Office of Scientific Research
European Office of Aerospace Research and Development
Unit 4515 Box 14, APO AE 09421

REPORT DOCUMENTATION PAGE

PLEASE DO NOT RETURN YOUR FORM TO THE ABOVE ORGANIZATION.

1. REPORT DATE	**2. REPORT TYPE**	**3. DATES COVERED**	
20220124	Final	**START DATE** 20180930	**END DATE** 20210929

4. TITLE AND SUBTITLE
Improvement of Physical Modeling for Vortex-Dominated Flows

5a. CONTRACT NUMBER	**5b. GRANT NUMBER**	**5c. PROGRAM ELEMENT NUMBER**
	FA9550-18-1-7019	61102F
5d. PROJECT NUMBER	**5e. TASK NUMBER**	**5f. WORK UNIT NUMBER**

6. AUTHOR(S)
Andreas Krumbein

7. PERFORMING ORGANIZATION NAME(S) AND ADDRESS(ES)
DEUTSCHES ZENTRUM FUR LUFT- UND RAUMFAHRT E.V.
LINDER HOHE
KOLN, NORDRHEIN-WESTFALEN 51147
DEU

8. PERFORMING ORGANIZATION REPORT NUMBER

9. SPONSORING/MONITORING AGENCY NAME(S) AND ADDRESS(ES)	**10. SPONSOR/MONITOR'S ACRONYM(S)**	**11. SPONSOR/MONITOR'S REPORT NUMBER(S)**
EOARD UNIT 4515 APO AE 09421-4515	AFRL/AFOSR IOE	AFRL-AFOSR-UK-TR-2022-0019

12. DISTRIBUTION/AVAILABILITY STATEMENT
A Distribution Unlimited: PB Public Release

13. SUPPLEMENTARY NOTES

14. ABSTRACT
In this work the advantages of applying Reynolds stress models over the eddy-viscosity RANS turbulence models and scale-resolving simulation methods for the flows characterized by separation from smooth surfaces and subsequent vortex formation are explored. To this end, the flow over a spheroid, a delta wing and a diamond wing, which all exhibit vortex separation, are investigated. For all the aforementioned configurations, predictions obtained by different approaches are compared to each other and to experiments. In this report, first, improvements and detriments observed in Reynolds stress model predictions compared to other RANS predictions are presented. Later, the performance of a Reynolds stress model is compared to scale-resolving simulations of hybrid RANS/LES type, and the predictive capabilities of the different methods and their advantages for the aforementioned flows

15. SUBJECT TERMS

16. SECURITY CLASSIFICATION OF:			**17. LIMITATION OF ABSTRACT**	**18. NUMBER OF PAGES**
a. REPORT	**b. ABSTRACT**	**c. THIS PAGE**		
U	U	U	SAR	48

19a. NAME OF RESPONSIBLE PERSON	**19b. PHONE NUMBER** *(Include area code)*
DOUGLAS SMITH	314 235 6013

DLR IB-XXX

Improvement of physical modeling for vortex separated flow

DA9550-18-1-7019

FINAL REPORT

DLR

Improvement of physical modeling for vortex separated flows

Report Details

Title	**Improvement of physical modeling for vortex separated flow**
Award Number	DA9550-18-1-7019
Report Type	Final report
Principal Investigator	
Authors	V. Togiti, A. Krumbein, A. Probst
Recipient Organization	Deutsches Zentrum fuer Luft-und Raumfahrt
Report Due Date	29th December 2021
Report period	30th September 2018 to 30th September 2021

Abstract

In this work the advantages of applying Reynolds stress models over the eddy-viscosity RANS turbulence models and scale-resolving simulation methods for the flows characterized by separation from smooth surfaces and subsequent vortex formation are explored. To this end, the flow over a spheroid, a delta wing and a diamond wing, which all exhibit vortex separation, are investigated. For all the aforementioned configurations, predictions obtained by different approaches are compared to each other and to experiments. In this report, first, improvements and detriments observed in Reynolds stress model predictions compared to other RANS predictions are presented. Later, the performance of a Reynolds stress model is compared to scale-resolving simulations of hybrid RANS/LES type, and the predictive capabilities of the different methods and their advantages for the aforementioned flows are discussed.

Contents

Table of figures

Introduction

Significant enhancements in computational fluid dynamics (CFD) have led to the use of numerical simulation in the design process of both civil and military aircraft, especially for nominal cruise performance where flows are generally characterized by attached flows. However, military vehicles routinely operate well outside of the steady, attached flow regimes often dominated by separated vortex flows. Therefore, major effort has to be devoted to ensure the vehicle qualified at many states that contain unsteady, highly separated flows. State-of-the-art CFD methods lack the ability to predict onset and progression of separated vortex-dominated flows, especially from smooth surfaces. Investigations carried out in several AVT task groups of the NATO Science and Technology Organization (STO) [1] indicate that the shortcomings for these predictions mainly stem from deficiencies of the models of turbulence. In most numerical investigations for slender wings with low sweep angle and blunt leading edges [2] linear eddy-viscosity turbulence models are employed. These models tend to deliver acceptable predictions at moderate incidence angles. However, at higher incidence angles, force coefficients and pitching moments were observed to be off compared to experiments. This is due to incorrect (earlier or delayed) prediction of incipient separation and differences in the strength of the subsequent development of vortices.

The linear eddy-viscosity models (EVM) are still the backbone of numerical simulations for industrial applications due to their numerical robustness. While being fairly reliable for attached boundary-layer flows, they often tend to fail in the case of flow separation. Furthermore, they are known to dissipate vortices too rapidly. The reason for the above failures of EVMs can be attributed to the underlying Boussinesq hypothesis, assuming the Reynolds stresses being parallel to the strain rate tensor, and to the discretized numerical representation of the Reynolds stresses in a code. Furthermore, the production terms of the underlying transport equations for the turbulent quantities need modeling. In contrast to EVMs full differential Reynolds stress models (RSM) provide individual transport equations for the Reynolds stresses. Its terms also have to be modeled, except for the production term which is treated exactly. For this reason, differential Reynolds stress models are considered particularly suitable for vortex-dominated flows. Investigations conducted in [3] [4] demonstrate the applicability of RSM for vortex dominated flows.

Vortex separated flows often are mildly or massively separated and highly unsteady. Numerical investigations of such flows involving complex flow phenomena often may not be well predicted by advanced RANS models, including RSM, and may require scale-resolving simulations (SRS) in which a small portion of turbulence is modeled and the rest is resolved. However, such methods require more computational resources compared to pure RANS simulations.

In this work, the objective is to demonstrate the capabilities of advanced turbulence models for the flows involving separation from a smooth body and subsequent vortex formation. To this end, first, the capabilities of a Reynolds stress model for vortex separated flows are evaluated. Later, scale-resolving hybrid RANS/LES simulations based on eddy-viscosity-models are

employed to the aforementioned flows and the advantage of applying such methods over Reynolds stress models is assessed. And finally, hybrid RANS/LES simulations based on a Reynolds stress model are used and benefits of this method over the eddy-viscosity-based SRS are evaluated.

Details of the investigated configurations

In the current study the flows over a spheroid, a delta wing, and a diamond wing are investigated. These configurations unveil separation from a smooth surface and subsequent vortex formation. The flow over a spheroid at high incidence exhibits a three-dimensional cross flow separation and subsequent formation of longitudinal vortices, see Figure 1(a). Strength and location of these vortices determine the maneuver characteristics of the body. Therefore, the accurate prediction of flow separation and vortex strength are of the greatest importance to determine forces and moments exerted on the body. In the present work, the flow over a 6:1 prolate spheroid is investigated at a Reynolds number based on the streamwise length of the spheroid, L, of $Re_L = 4.2x10^6$ and a Mach number of 0.2 at the incidence of $\alpha = 20^o$, based on the experimental investigations of [5]. As in the experiments, transition is set at x/L = 0.2 on both windward and leeward sides of the spheroid.

The other case investigated is the flow over the delta wing based on the experimental investigations carried out in the Vortex Flow Experiment-2 [6] at the DLR Göttingen. In the experiments, a 65^o swept delta wing configuration with different rounded and sharp leading edges at angles of attack of 13.3^o and 18^o was investigated. In the experiments at the former incidence angle a partially developed separated vortex flow was observed while at the latter incidence angle a fully developed separated vortex flow was observed. In the current study the partially developed separated vortex flow case at a freestream Reynolds number based on the mean aerodynamic chord (c_{mac}) of $3x10^6$ and Mach number of 0.4 and the incidence angle of 13.3^o with a medium radius rounded leading edge of $r/c_{mac} = 0.15\%$ is investigated. The flow topology at the aforementioned incidence angle is displayed in Figure *1* (b) which unveils vortex separation, inner and outer primary vortices.

The other case investigated is the flow over a diamond wing which is based on the experimental study conducted in the NATO/AVT-183 task group [7] [8]. The geometry is a diamond wing with leading and trailing-edge sweeps of 53^o and -26.5^o, respectively. In the experiments, the geometry is mounted on a tunnel floor wall with a peniche with standoff distance of $0.075c_r$, where c_r is the root chord which is 1.2m and tests were conducted at a free stream Mach number of 0.15 and Reynolds number based on the mean aerodynamic chord of $2.7x10^6$ and the incidence angle range of 10^o to 15^o with an increment of 1^o. For the present numerical investigation, the incidence angle of $\alpha = 12^o$ was chosen as the flow separates midway along the blunt leading edge. Global flow field characteristics associated to the incidence angle of 12^o are depicted in Figure *1*(c) which displays flow separation and the inner and outer primary vortices.

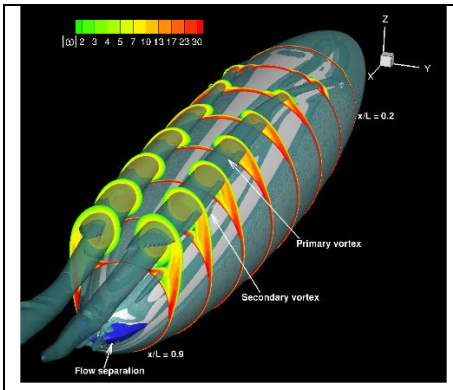

(a) Spheroid

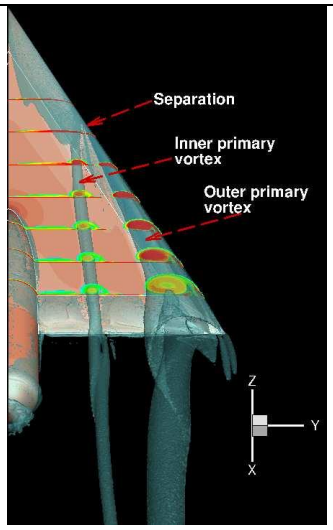

(b) Delta wing

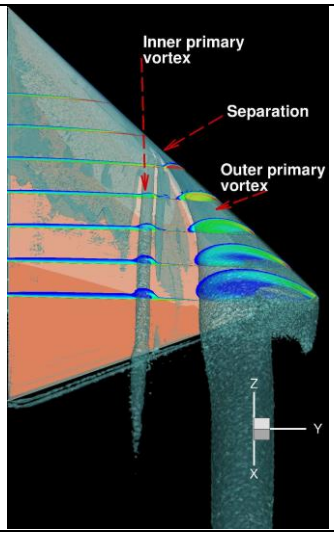

(c) Diamond wing

Figure 1: Flow topology on different configurations.

Turbulence modeling

Separated vortex flows investigated in the current study involve separation from a smooth body surface and the formation of vortices. Often the vortex interaction with the attached boundary layer exposed to an adverse-pressure gradient leads to secondary vortices where anisotropy of normal Reynolds stresses is observed in experimental investigations [5]. Over the years, extensions to EVMs have been introduced to improve predictions of vortex flow and normal Reynolds stress anisotropy. In the present study EVMs coupled to a rotational correction (RC) approach [9] and the Quadratic Constitutive Relation (QCR) [10] which improve the prediction of the vortex strength and the anisotropy of normal Reynolds stresses are employed. For the present study the Spalart-Allmaras one-equation [11] and the Menter SST k-ω [12] turbulence models are considered. In the present study both models coupled to RC and QCR are employed and in the discussion they are denoted as SA-RC-QCR and SST-RC-QCR.

Concerning RSMs, often the application of differential RSMs to flows involving complex flow phenomena leads to numerical stability problems due to numerical stiffness. This may be one of the reasons for not carrying out investigations with differential RSM in the earlier AVT studies [1]. Recently at DLR, a mathematically exact transformation of the length-scale-providing equation coupled to RSM was studied and demonstrated that such a transformation can significantly improve the stability of RSM for complex industrial flows. In the current study, the SSG/LRR Reynolds stress model [13] developed at DLR within the FLOMANIA project is considered. The ln(ω) length-scale equation [14] coupled to SSG/LRR-RSM, which improves the stability of RSM for complex flows, is employed in the current study and in the discussion the model predictions are denoted RSM.

As one of the objectives is to assess scale-resolving simulation (SRS) methods for flows involving separation from a smooth surface and subsequent vortex formation, eddy-viscosity-based SRS

methods are considered. Here the SA- and SA-RC-QCR-based delayed detached eddy simulation (DDES) [15] are considered. This approach combines RANS and LES in a way that in attached flow regions RANS is applied and in the separated regions large-eddy simulation (LES) is employed. The advantage of such a method is that flows involving massive separation and highly unsteady in nature are more accurately predicted compared to standard RANS approaches at a reasonable computational effort.

In the current investigation the test cases investigated demonstrate partially separated flow and this makes the accurate prediction of such flows with hybrid RANS-LES methods, here the DDES approach, challenging. In the discussion the results obtained by the DDES based on the SA and SA-RC-QCR are denoted SA-DDES and SA-RC-QCR-DDES, respectively.

Later, the DDES based on RSM is employed for the investigations. In this approach, analogously to the SST-DDES [16], the dissipation term in the Reynolds stress transport equation is modified for DDES. Here, the isotropic dissipation term is multiplied by the ratio of RANS and DDES length scales. In near-wall regions, the ratio of the length scale is one where the model acts as pure RANS. In separated regions, the length scale ratio is larger than one, where the DDES length scale is smaller than the RANS length scale. Due to this, the dissipation term increases and thereby reduces the modeled Reynolds stresses, which allows resolving turbulence. Details pertaining to RSM-based DDES can be found in [17]. The results obtained by this variant of DDES is denoted by RSM-DDES in the discussion. In the present work, with the RSM-DDES, switching between RANS to LES is done using Menter's blending function F1 [12] in order to resolve vortices located very close to wall.

Numerical methods

In the current investigation the unstructured compressible DLR flow solver TAU is used. Details about the DLR TAU code can be found in [18]. The inviscid fluxes of the main-flow equations are calculated by a central scheme with matrix artificial dissipation. For the turbulence equations, the convective fluxes are approximated with a second-order Roe scheme in the RSM and RSM-based DDES investigations and an Average-of-flux scheme in SA-RC-QCR and SA-RC-QCR-based DDES investigations. The viscous fluxes of the main flow and the diffusion fluxes of the turbulence equations are discretized using central differences.

For the DDES computations, low numerical dissipation is required in order to avoid excessive damping of resolved turbulent structures. In the current work, for the SA-DDES and SA-RC-QCR-DDES investigations the hybrid low-dissipation/low-dispersion (LD2) scheme is used, details can be found in [19]. However, for the RSM-DDES, such low dissipation leads to energy accumulation at high wave-numbers for the decaying isotropic turbulence case. In order to obtain the correct energy decay, the numerical dissipation is increased slightly, for details see [17].

For RANS investigations, steady computations are performed using a semi-implicit lower-upper symmetric Gauss-Seidel (LUSGS) method. For SRS and unsteady RSM computations, time-accurate computations are carried out with a 2^{nd}-order dual time-stepping scheme.

In the present study, steady computations are performed with all the RANS turbulence models for the spheroid configuration. For the delta wing and diamond wing, steady computations are performed with the SA-RC-QCR. However, with the RSM oscillatory force coefficients are observed in steady computations and hence time-accurate computations are carried out with a non-dimensional time step size of 0.01, which is about $1/100^{th}$ CTU (CTU: convective time unit calculated from wing root chord length and reference velocity; c_r/U_{ref}), until the force coefficients flatten out. In the current investigations, the computations are run for about 8 to 10 convective time units.

Performance evaluation of RSM

Since the objective is to evaluate the predictive capabilities of an RSM model formulation for separated vortex flows, investigations are carried out for the flow over a spheroid, delta wing and diamond wing. All the test cases demonstrate separation from a smooth body surface and subsequent vortex formation. Here, the challenge is the accurate prediction of incipient separation and the strength of the vortices. To evaluate the performance, predictions are compared with available experimental data and EVM predictions.

Spheroid

The flow over a prolate spheroid at the incidence of α = 20° is investigated. Here, first, grid refinement and grid topology investigations are carried out, and later performance studies are conducted.

Grid refinement study

To keep spatial discretization errors on the predictions as low as possible, a grid refinement study is performed using RSM. For this purpose, two grid types with varying resolution from very coarse to fine are created and employed here. One grid family is a completely hexahedral one and the other is a hybrid grid family consisting of hexahedrons in the near-wall region and tetrahedrons in the remainder of the computational domain. A depiction of the two grid types is shown in Figure *2*. Details of the grid resolution are given in the Table 1.

Table 1 Grid details for the spheroid test case. Number of points in millions.

Grid	Very coarse	coarse	Medium	Fine
Hexahedra	0.12	1	7.5	61
hybrid (SOLAR)	-	3.8	11.4	35.5

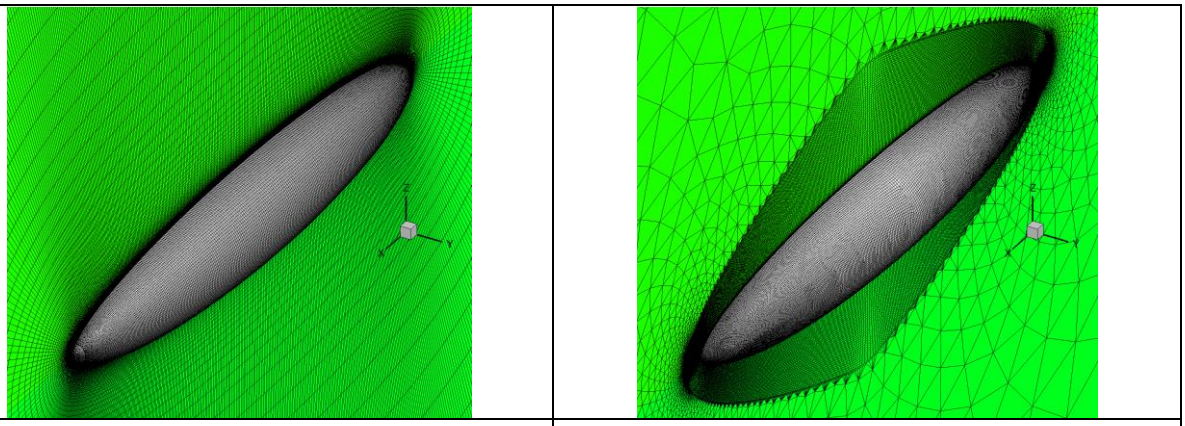

(a) Hexa grid | (b) Hybrid grid

Figure 2: Overview of hexahedron and hybrid grids for the spheroid.

The grid convergence of the force coefficients delivered by RSM is shown in Figure *3*. On both grid types convergence of lift and drag with the refinement of the grid is within reach. On the last two fine grids, almost identical force coefficients are obtained on the hexahedra and hybrid grids and the results on the finest grids are almost independent of the grid type.

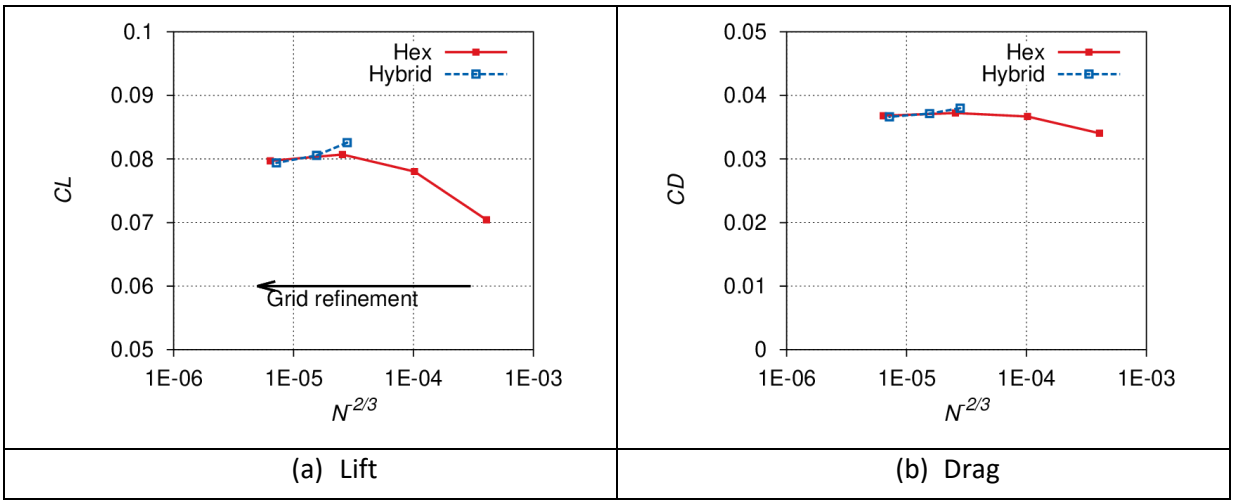

(a) Lift | (b) Drag

Figure 3: Grid refinement study on hexahedra and hybrid grids for the spheroid.

A comparison of the pressure coefficient distributions at two different streamwise sections obtained on different hexahedra grid levels is shown in Figure 4. Here, the cp along the azimuthal direction from windward side to leeward side of the spheroid is shown, the direction is shown in Figure 4(b). On all the grids, flow acceleration up to $\varphi = 90°$ is predicted. Beyond this location, flow separation and the subsequent formation of a primary vortex occur. The local cp_{min} in the range $135° < \varphi < 180°$ represents the pressure distribution associated with the primary vortex location. As can be seen, the local cp_{min} is not predicted on the very coarse grid due to the weak vortex in the simulation. However, as the grid is refined the vortex strength increases and the local cp_{min} exhibits stronger peaks. On the medium and fine grids almost

identical cp_{min} is predicted and overall the cp on both medium and fine grids does not change significantly with grid refinement.

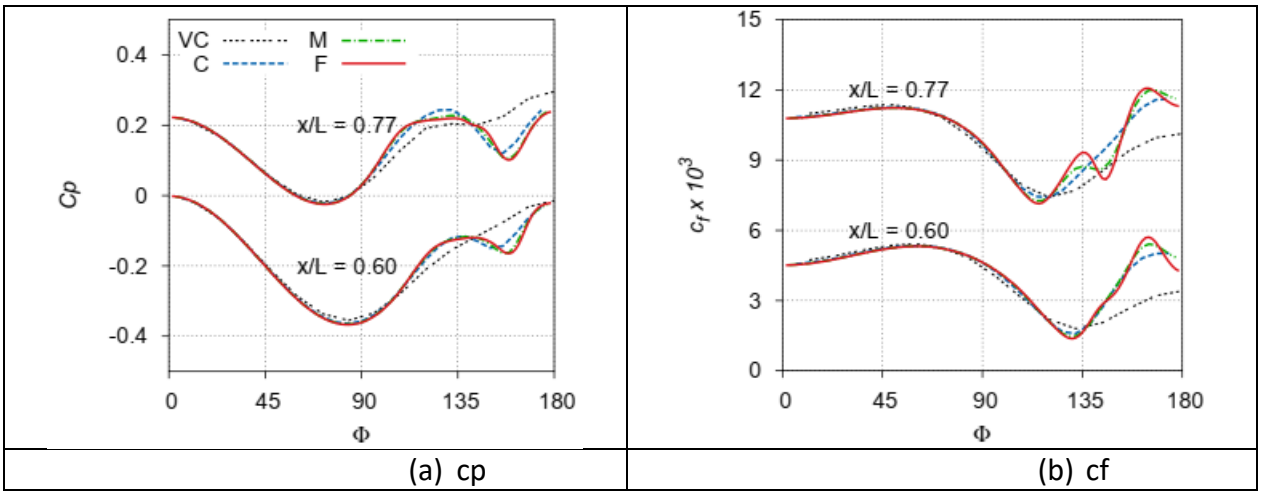

(a) cp (b) cf

Figure 4: Grid refinement on hexahedra grid for the spheroid. VC: very coarse, C: coarse, M: medium and F: fine.

In Figure 4(b) the cf distribution at two different streamwise sections is shown. Local cf_{min} and cp_{max} represent flow separation and reattachment, respectively. At x/L = 0.6, flow separation is predicted almost at the same location on all grids. However, reattachment is not clear on the very coarse grid due to the weakness of the vortex. On the other grids, reattachment is predicted almost at the same location. At x/L = 0.77, primary separation and reattachment are predicted at the same locations on the coarse to fine grids. Minor differences are observed in the location of secondary separation and reattachment. On the very coarse and coarse grids, the secondary separation is not predicted and, thus, local cf_{min} and cf_{max} are not observed in the region $110° < \varphi < 150°$. On the medium and fine grids, the secondary flow separation and reattachment are predicted at the same locations. However, differences are observed in the local cf_{max} which is due to the stronger secondary vortex observed on the fine grid. Overall, the qualitative and quantitative similarity in the results of cp, cf, lift and drag on the medium and fine hexahedra grids indicate that grid converged results are within reach.

In Figure 5 (a), cp and cf obtained on the fine hexahedra and hybrid grids are compared. On both grids almost identical pressure and very close skin-friction distributions are predicted by the RSM. A comparison of the contours of the vorticity magnitude and the turbulent kinetic energy (both not shown here) unveiled again almost identical distributions. Overall, the RSM delivered almost identical or matching results on the fine grids independent of the grid topology. For the further studies, only the fine hexahedra grid is employed.

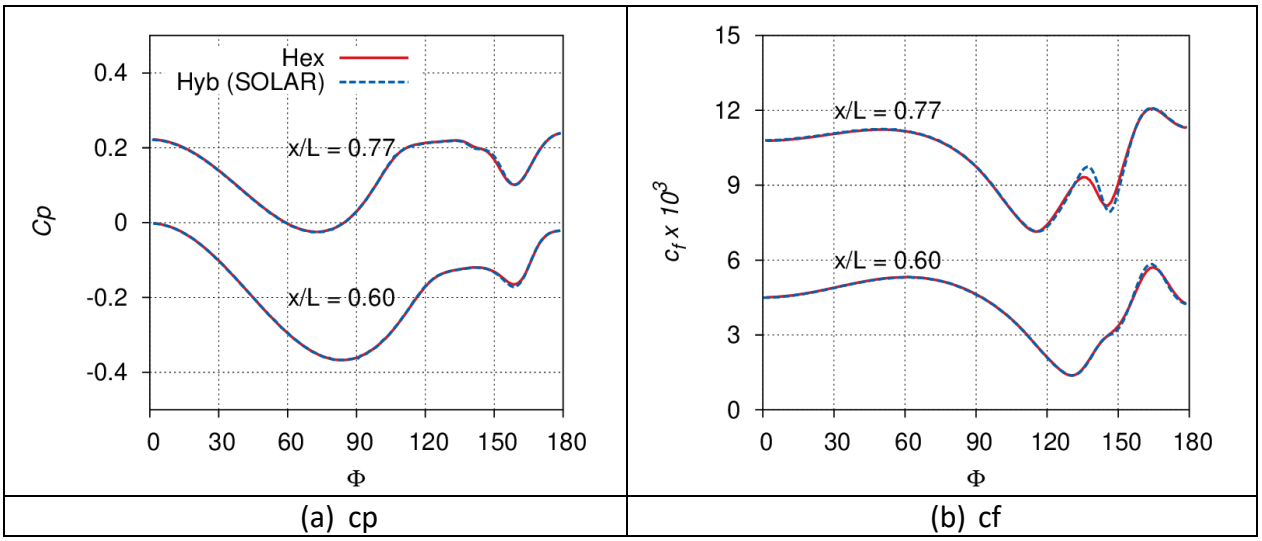

(a) cp (b) cf

Figure 5: Grid topology study on hexahedra and hybrid grids for the spheroid.

Turbulence model study

To evaluate the performance of turbulence models, investigations are carried out with the SA-RC-QCR, SST-RC-QCR and RSM turbulence models and the predictions are compared to the available experimental data [5].

In Figure 6 (a), the surface pressure distribution along the azimuthal direction at streamwise locations of x/L = 0.6 and 0.77 are shown. In the experiments the local cp_{min} in the region of $135° < \varphi < 180°$ indicates the location of the primary vortex. In all the predictions the primary vortex location is observed slightly inboard compared to the experiments. The pressure associated with the primary vortex is underpredicted with all the turbulence models applied. A possible reason for this discrepancy is the weaker vortex compared to the experiments.

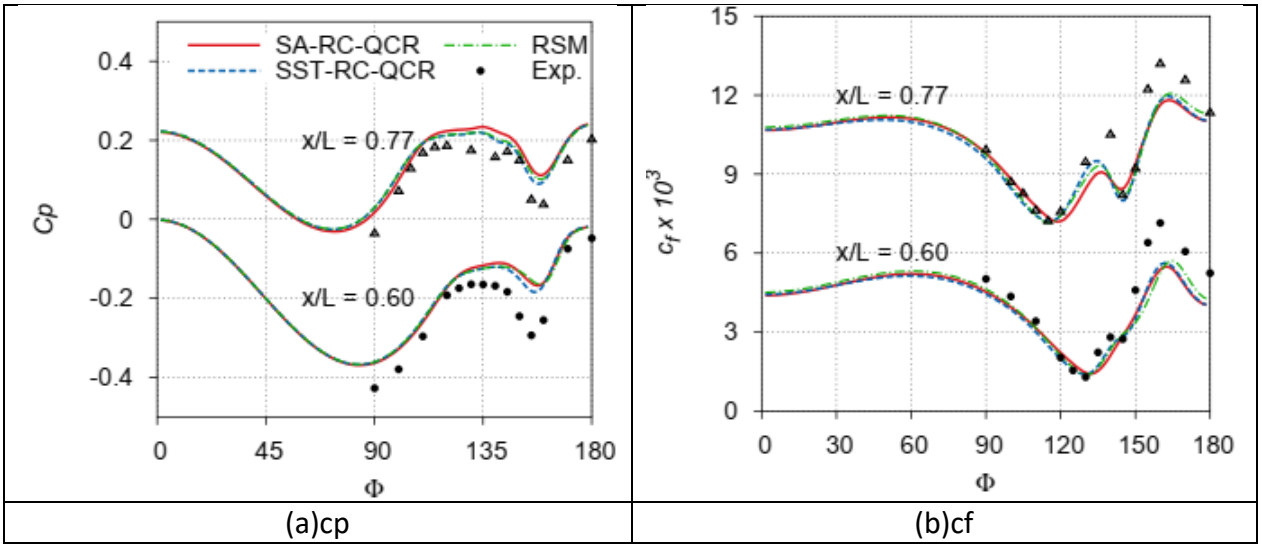

(a)cp (b)cf

Figure 6: Turbulence model study for the spheroid on the hexahedra fine grid.

The pressure plateau in the experiments in the region of 112° < φ < 145° at x/L = 0.6 and 100° < φ < 135° at x/L = 0.77 unveils the extent of separated flow. All the models deliver almost similar pressure levels in the separated region and the results exhibit a satisfactory agreement with the experiments.

In Figure 6(b), cf along the surface in the azimuthal direction at two different streamwise locations is shown. In the experiments local cf_{min} and cf_{max} indicate local flow separation and reattachment, respectively. At x/L = 0.6 all the models reproduce the experimental separation location. At x/L = 0.7, local cf_{min} is observed at two locations in the experiments. At φ = 120° the local cf_{min} represents the primary separation and at φ = 140° local cf_{min} unveils a secondary separation. In the case of SA-RC-QCR the primary separation is slightly delayed whereas the RSM and SST-RC-QCR deliver the experimental separation point. Concerning the secondary separation, all the models reproduced the experimental secondary separation point. The cf_{max} denotes the region close to flow reattachment. In the region 150° < φ < 180°, compared to the experiments, the reattachment is predicted inboard with all the turbulence models. Again, the cf_{min} level is underpredicted which is linked to the vortex strength that is underpredicted.

Contours of the vorticity magnitude delivered by different turbulent models at x/L= 0.77 is shown in Figure 7. As can be seen, all the applied turbulence models predict almost the same level of vorticity magnitude in the separated shear layer and in the secondary vortex region. In the core of the primary vortex, minor differences can be observed. In the RSM and SST-RC-QCR slightly higher vorticity magnitude values are predicted compared to the SA-RC-QCR. This marginally lower vorticity magnitude in the SA-RC-QCR predictions lead to marginally higher pressure on the surface in the region of the primary vortex, see Figure 7(a).

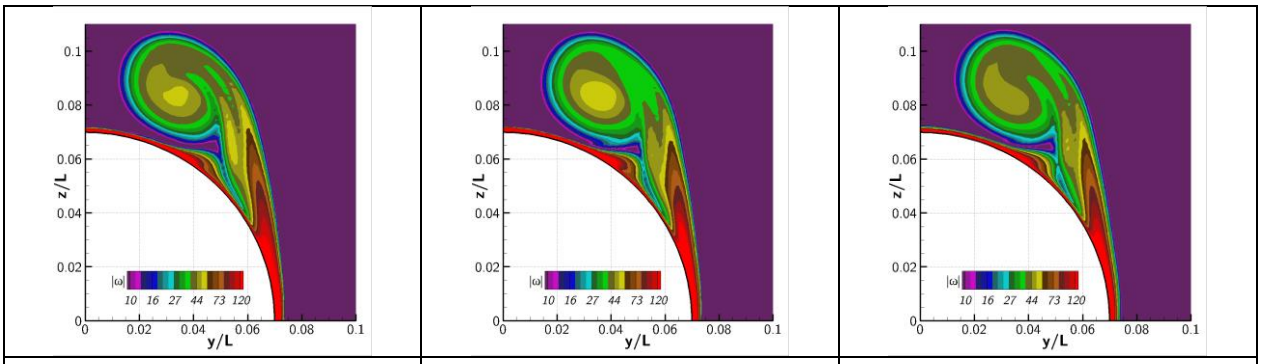

(a) RSM | (b) SST-RC-QCR | (c) SA-RC-QCR

Figure 7: Contours of vorticity magnitude on the spheroid at x/L = 0.7.

In Figure 8, contours of turbulent kinetic energy (TKE) are shown. In the separated shear layer the predicted values show a still acceptable agreement with the experiment, although one can doubt the quality and reliability of the measured data and, thus, a more profound assessment is not possible. In the region where the shear layer from the secondary separation interacts with the free shear layer emanating from the primary separation, very high TKE is observed in the experiments. This trend is reproduced in SST-RC-QCR and RSM and the predicted value levels agree well with the experimental data.

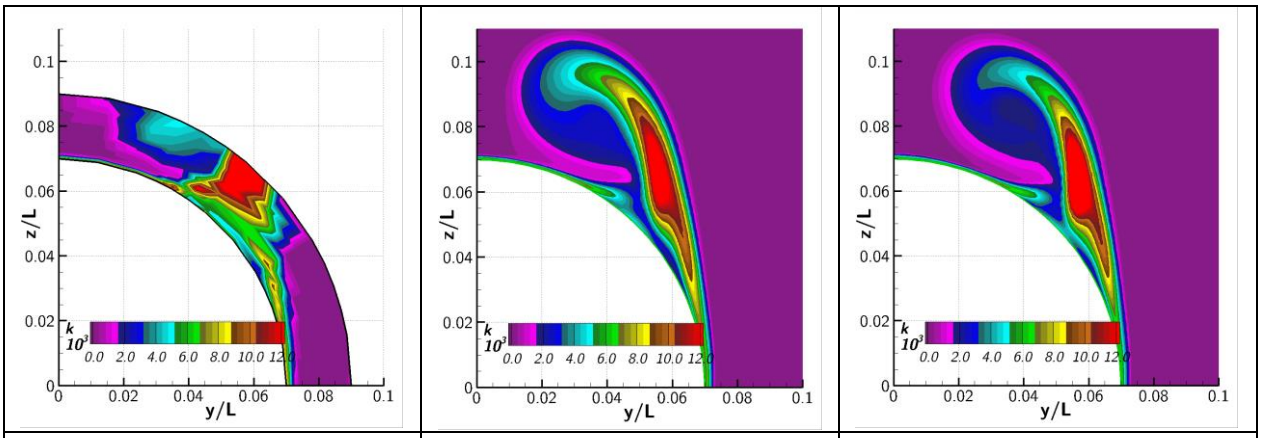

(a) Exp.	(b) RSM	(c) SST-RC-QCR

Figure 8: Contours of turbulence kinetic energy on the spheroid at x/L = 0.7722.

To visualize the resolved vortices, the iso-surface of the vortex criterion λ_2 is shown in Figure 9. As can be seen all the applied models resolve both primary and secondary vortices well. To unveil the separated region, the iso-surface of the streamwise velocity is also shown with blue color in the same figure. From the figure it is evident that all the models predict almost the same size of separation at the base of the spheroid.

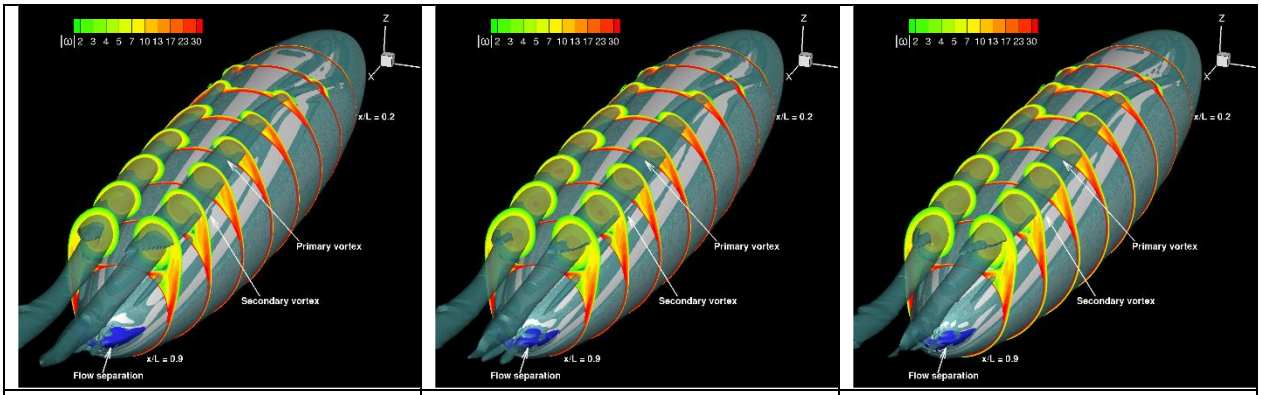

(b) RSM	(b) SST-RC-QCR	(c) SA-RC-QCR

Figure 9: Iso-surface of λ_2 = -1 and streamwise velocity u = 0 for the spheroid.

Overall, all the applied models deliver almost similar predictions and the results are observed to be in good agreement with the experimental data. EVMs when coupled with RC and QCR tend to deliver predictions of very similar qualitative and quantitative levels as a full differential RSM for the current test case. Differences in cp and cf in the primary and secondary vortex regions may be emanating from the differences in vortex strength. In the current investigation, grid refinement studies showed that not much improvement can be observed by further grid refinement. It may be that further improvement of physical modeling is required to improve vortex strength.

Delta wing

The second test case considered is the flow over a swept delta wing with round leading edge. For this test case, first, a grid refinement study is carried out and later a turbulence model study

is conducted to evaluate the turbulence model performance. Finally, the effect of the free stream Reynolds number is investigated for the same geometry.

For the present study, the Centaur grid generation tool was used to generate grids. Three grids successively refined both in boundary-layer and far-field regions were generated. The coarse grid has 6 million points while the medium and fine grids have 15 and 44 million points, respectively. To study the grid topology effect, another grid with hexahedra cells in the near-wall region and tetrahedra cells in the far-field is generated using the SOLAR grid generation tool.

Grid refinement study

A grid refinement study is carried out using the RSM. The effect of grid resolution on the predicted flow topology is assessed based on the surface pressure distribution. In Figure 10, the contours of the pressure coefficient distribution on the surface along with surface skin-friction lines are shown. On all grid levels flow separation from the leading-edge occurs at x = 0.4 which is denoted by the region of low cp moving from the round leading-edge to the inboard section of the wing. On all grids, the inner primary and outer primary vortices are resolved. On the coarse grid a second outer primary vortex is predicted on the coarse grid which can be seen at x = 0.7. However, on the finer grids this trend is not observed.

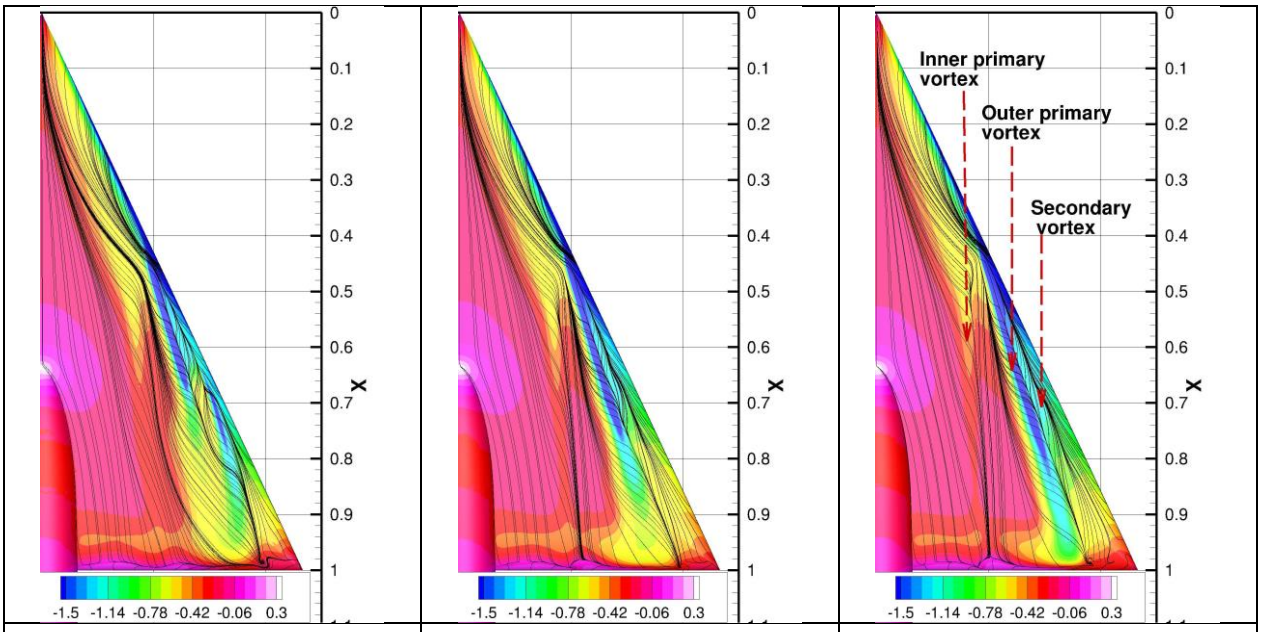

(a) Coarse (b) Medium (c) Fine

Figure 10: Surface pressure distribution and skin-friction lines on the delta wing for different grid levels.

Further differences can be seen in the pressure distribution associated with the vortices on different grid levels. The region with low pressure associated with the outer primary vortex is extended in streamwise direction with the grid refinement. The reason for this trend is the

vortex strength which increases as the grid is refined. On the medium and fine grids, almost similar pressure distributions are predicted in the inner primary vortex region.

For a quantitative comparison, cp at different streamwise sections obtained on different grid levels is shown in Figure 11. Due to attached flow in the region upstream $x/c_r = 0.4$, almost identical pressure distributions are obtained on all grids. At $x/c_r = 0.6$, the suction peak at the spanwise location of $\eta = 0.85$ indicates the low pressure associated with the outer primary vortex core which is delivered almost identical on all the grids. Another local cp peak at the spanwise location of $\eta = 0.6$ renders the suction pressure associated with the inner primary vortex which is also almost identical on all the grids. However, at $x/c_r = 0.8$ differences in the suction pressure can be observed. On the coarse grid, the cp peak moves outboard which is due to a second primary vortex which is generated due to flow separation from the leading-edge. On the medium and fine grids, the outer primary vortex is located at the spanwise location of $\eta = 0.8$ and the suction peak associated with the vortex increases with the grid refinement due to stronger vortex on the finest grid. At $\eta = 0.9$, a higher suction peak on the finest grid is delivered.

Overall, on the medium and fine grids, almost the same pressure distribution for the inner primary vortex is observed. Concerning the outer primary vortex, the location of the outer primary vortex is observed at the same location on the medium and fine grids. For the further investigations the finest grid employed here is considered.

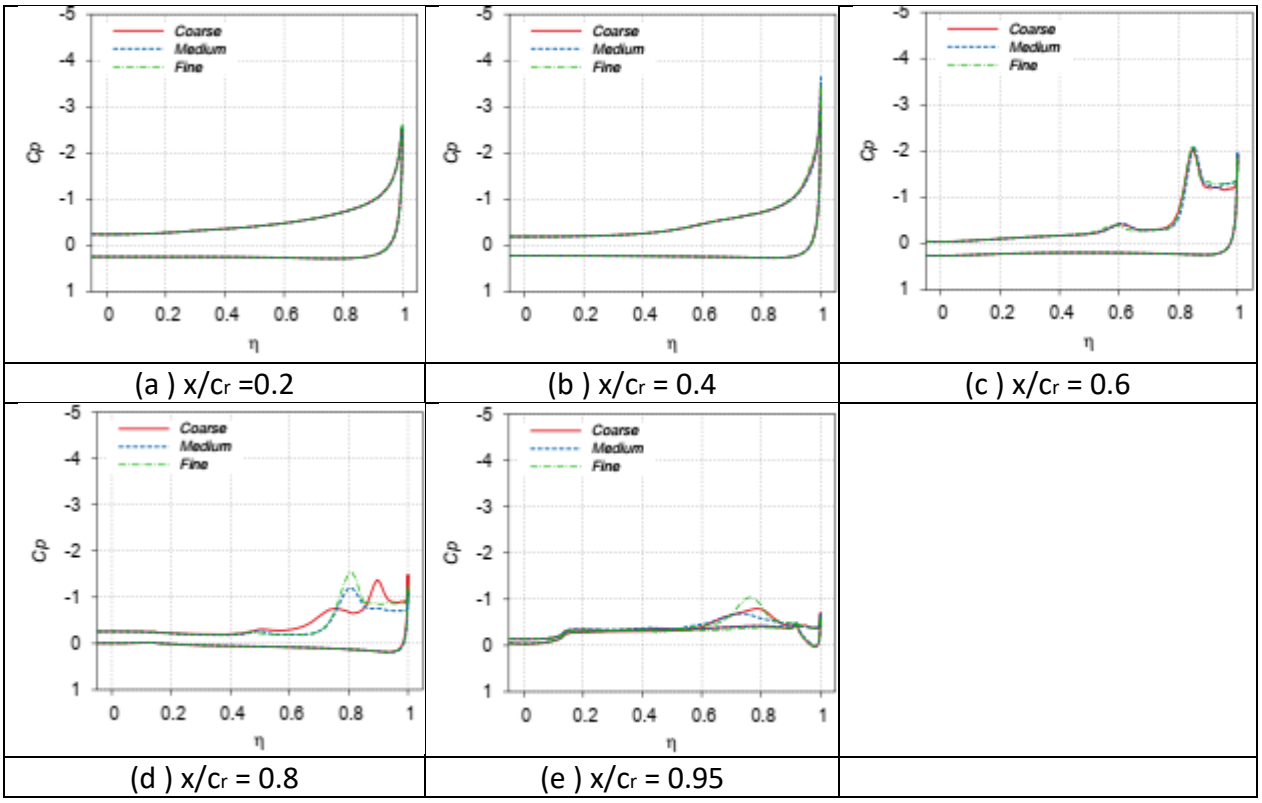

Figure 11: Pressure coefficient distribution for the delta wing on different grid levels.

Grid topology investigations

An additional grid generated using the SOLAR grid generation tool is employed to carry out grid topology investigations. On the SOLAR grid the surface is mainly resolved with quadrilateral cells and, as a result, the boundary-layer regions are resolved with hexahedra cells and the remaining region is filled with tetrahedra cells. The major difference between the Centaur hybrid and SOLAR hybrid grids is the near-wall grid topology. Here the main objective is to evaluate the influence of the near-wall cell types on the separated vortical flow. For this purpose, the SOLAR grid resolution is kept as close to the Centaur fine grid resolution as possible. The finest Centaur grid has a total number of points of 44 million while the SOLAR grid has 42 million grid points.

Surface pressure distributions and skin-friction lines obtained on the Centaur and SOLAR grids are shown in Figure 12. On both grids flow separation from the round leading edge is predicted almost at the same location x = 0.4 and resolved inner and outer primary vortices are present. Minor differences in the suction pressure associated with the vortices can be seen. On the SOLAR grid, the suction pressure is slightly lower compared to the Centaur grid. This is due to the marginally coarser far-field grid resolution leading to a weaker vortex strength compared to the Centaur grid. To demonstrate the minor differences in cp, sectional pressure distribution at x/c_r = 0.6, 0.8 and 0.95 are shown in Figure 13. As can be seen in the figure, the suction peak associated with the outer primary vortex is slightly lower on the SOLAR grid compared to the Centaur grid.

Based on the grids used in the current study, no great influence of the grid topology on the predictions is observed. For the further studies, the hybrid Centaur fine grid is used because it predicted a higher suction peak compared to SOLAR fine grid.

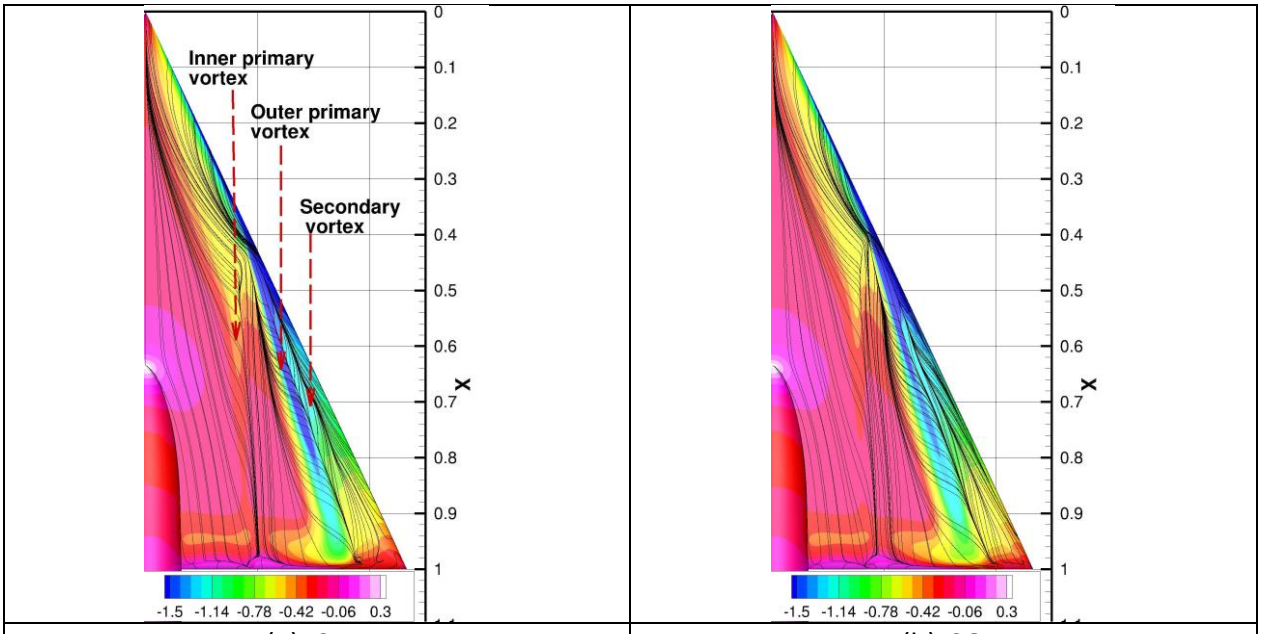

Figure 12: Pressure and coefficient and skin-friction lines on the delta wing on the fine.

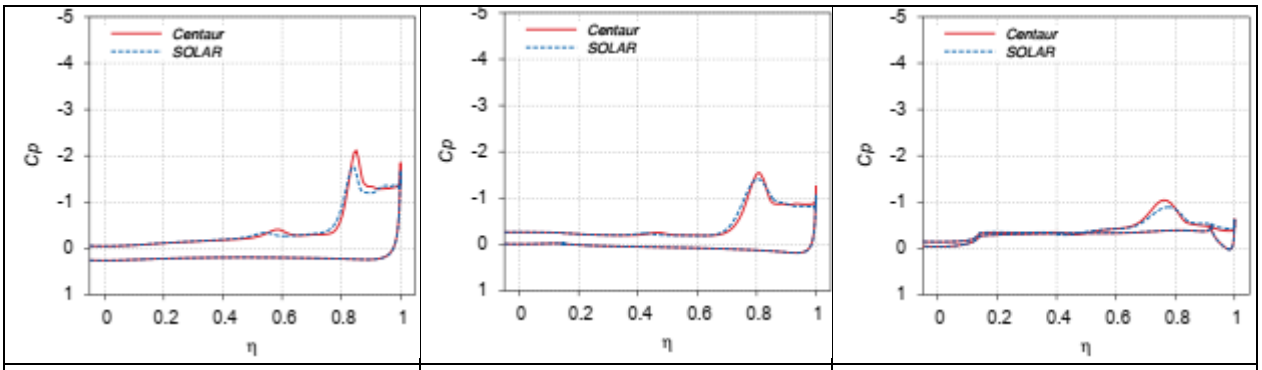

(a) $x/c_r = 0.6$ | (b) $x/c_r = 0.8$ | (c) $x/c_r = 0.95$

Figure 13: Influence of grid topology on pressure coefficient distribution for the delta wing.

Turbulence model study

To evaluate the turbulence model capabilities, investigations are carried out with the SA-RC-QCR and RSM on the fine Centaur grid. To unveil the resolved vortices, the iso-surface of λ_2 along with the vorticity contours at several streamwise locations are shown in Figure 14. Both the SA-RC-QCR and RSM resolve inner and outer primary vortices. From the contours of the vorticity magnitude in the inner primary vortex, it is evident that the resolved vortex is weaker compared the one delivered by RSM. The vorticity contours in the outer primary vortex unveil that both SA-RC-QCR and RSM predict almost the same vorticity magnitude up to $x/c_r = 0.8$. However, downstream of this location in the SA-RC-QCR predictions a low vorticity magnitude in the vortex is predicted. To display the effect of the vorticity magnitude on the pressure distribution, the contours of cp along with the skin-friction lines are shown in Figure 15. From the skin-friction lines it is evident that the SA-RC-QCR and RSM resolve both the inner and outer primary and secondary vortices. Downstream of $x/c_r = 0.8$, in the SA-RC-QCR the pressure associated with the outer primary vortex is higher compared to the RSM. This is due to weaker vortex predicted in the SA-RC-QCR as discussed earlier.

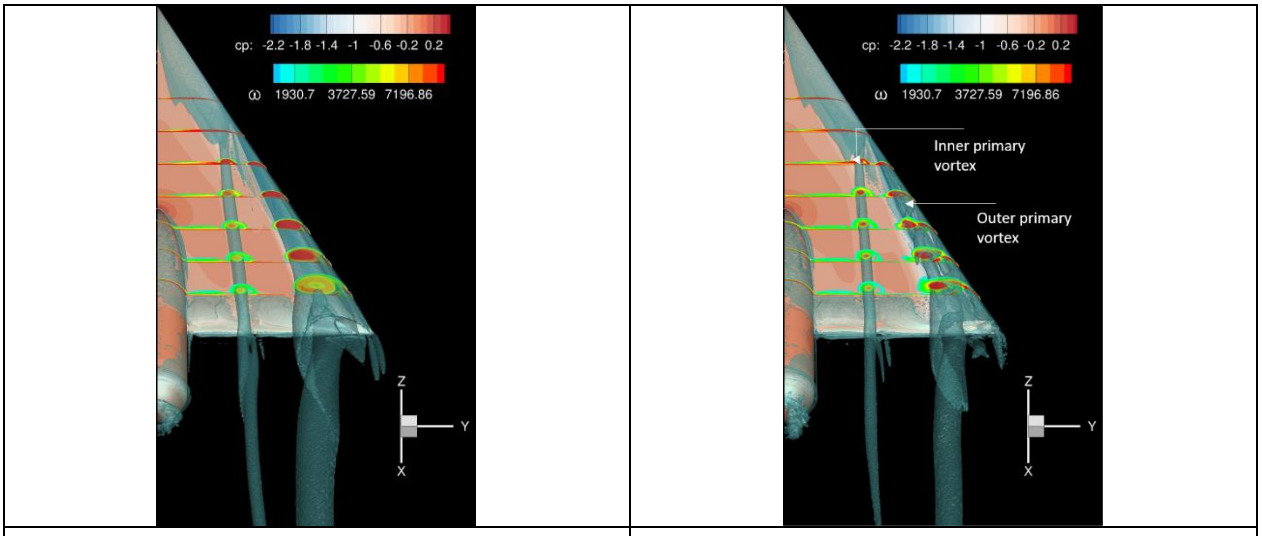

(a) SA-RC-QCR | (b) RSM

Figure 14: Iso-surface of λ_2 and the contours of vorticity magnitude delivered by SA-RC-QCR and RSM for the delta wing.

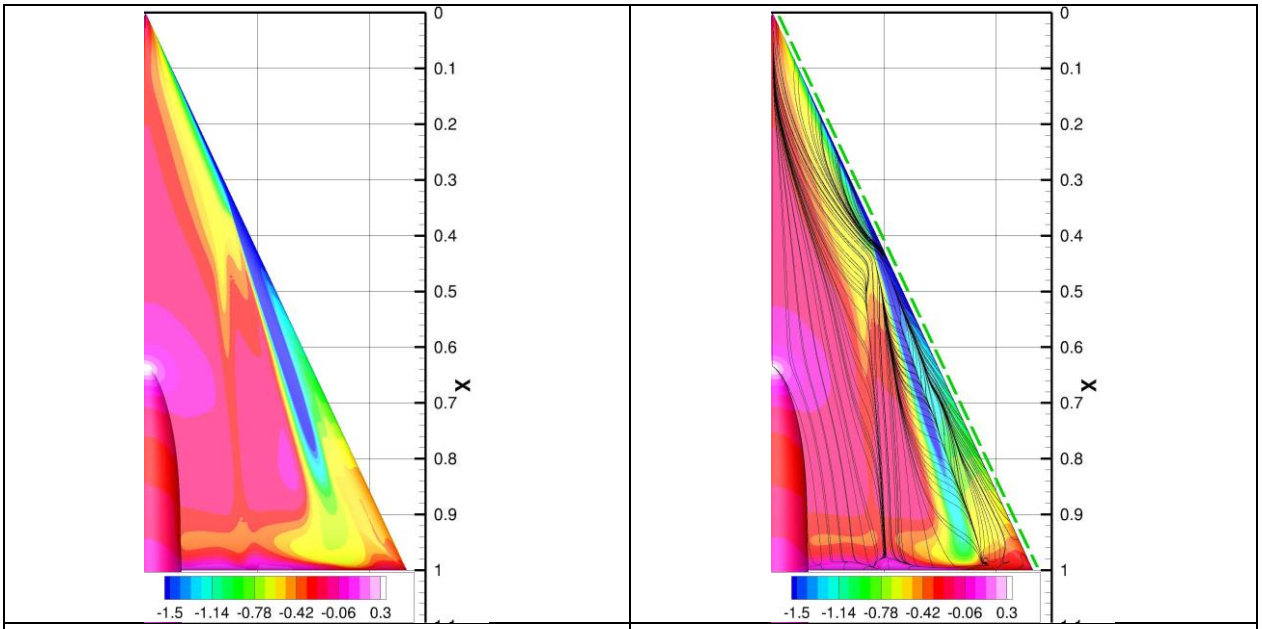

(c) SA-RC-QCR (d) RSM

Figure 15: Pressure and coefficient and skin-friction lines on the fine Centaur grid; turbulence model study for the delta wing.

To evaluate the performance of the applied turbulence models, sectional cp distributions delivered by the RSM and SA-RC-QCR are compared to the experimental data in Figure 16. At $x/c_r = 0.2$, both models predict attached flow and deliver almost identical pressure distribution and agree well with the experiments. At $x/c_r = 0.4$, the flow is still attached in the experiments. This trend is reproduced in the RSM predictions. However, in the case of SA-RC-QCR, the flow separation occurs upstream of this location and subsequent vortex formation begins. As a result, low pressure in the vortex core is exerted on the surface which is rendered in the cp spike at $\eta = 0.9$. This shows that in the SA-RC-QCR predictions flow separation occurs earlier than in the experiments which lead to a mismatch of cp with the experimental data at this location.

At $x/c_r = 0.6$ and 0.8, the suction peaks in the experimental pressure distribution indicate the location and associated pressure distribution of the inner primary and outer primary vortices. Low pressure associated with the outer primary vortex is predicted well with the SA-RC-QCR and RSM, however, the vortex is located too far inboard in the predictions. In the outboard separated region, $\eta > 0.9$, SA-RC-QCR delivers higher pressure compared to the experiments. The pressure distribution delivered by the RSM yields a clearly better agreement with the experimental cp. In the experiments, the inner primary vortex location and the associated pressure is rendered with the local cp_{min}. In the SA-RC-QCR and RSM predictions, the pressure associated with the primary vortex is underpredicted. Concerning the location, the SA-RC-QCR predicts the vortex too far inboard while RSM delivers the location which is in between

experiments and SA-RC-QCR predictions and, thus, closer to the experiments. At x/r = 0.95, in the SA-RC-QCR predictions an almost flat cp-distribution is delivered due to the weaker outer primary vortex whereas in the case of RSM cp associated with the outer primary vortex is reproduced as in the experiments.

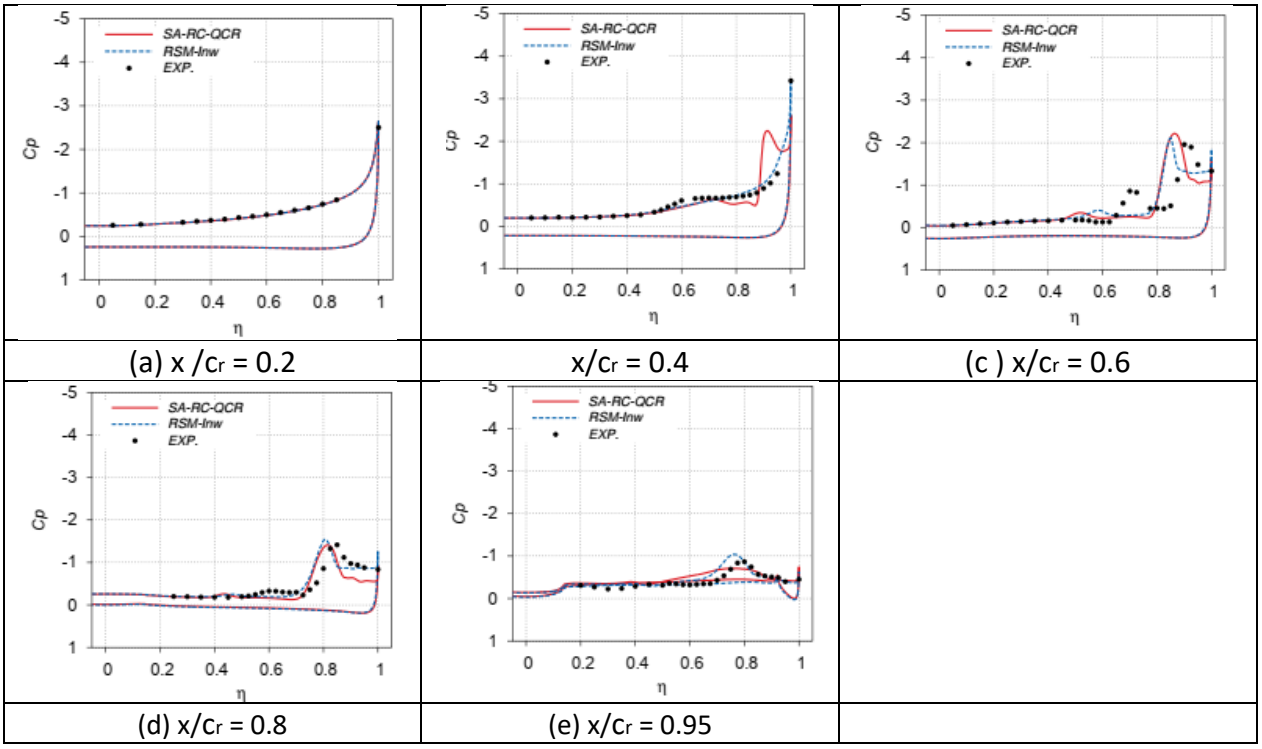

(a) x /c_r = 0.2 | x/c_r = 0.4 | (c) x/c_r = 0.6

(d) x/c_r = 0.8 | (e) x/c_r = 0.95

Figure 16: Pressure coefficient distribution delivered by SA-RC-QCR and RSM on the fine grid.

Overall, the RSM-based predictions are observed to be in better agreement with the experiments with respect to the separation location from the leading edge, pressure associated with the primary vortex and the separated region on the outboard section of the wing. However, still the remaining challenge is to accurately predict the inner primary vortex location and the pressure distribution associated with the vortex.

Since the RSM delivered better predictions compared to SA-RC-QCR, the further studies are carried out with the RSM.

Reynolds number study

To study the influence of the Reynolds number on the incipient separation and subsequent vortex formation, investigations were carried out at a freestream Mach number of 0.4 and a Reynolds number of 2 million, 3 million and 6 million at the incidence angle α = 13.3°. For this investigation, the finest Centaur grid used in the earlier studies is employed.

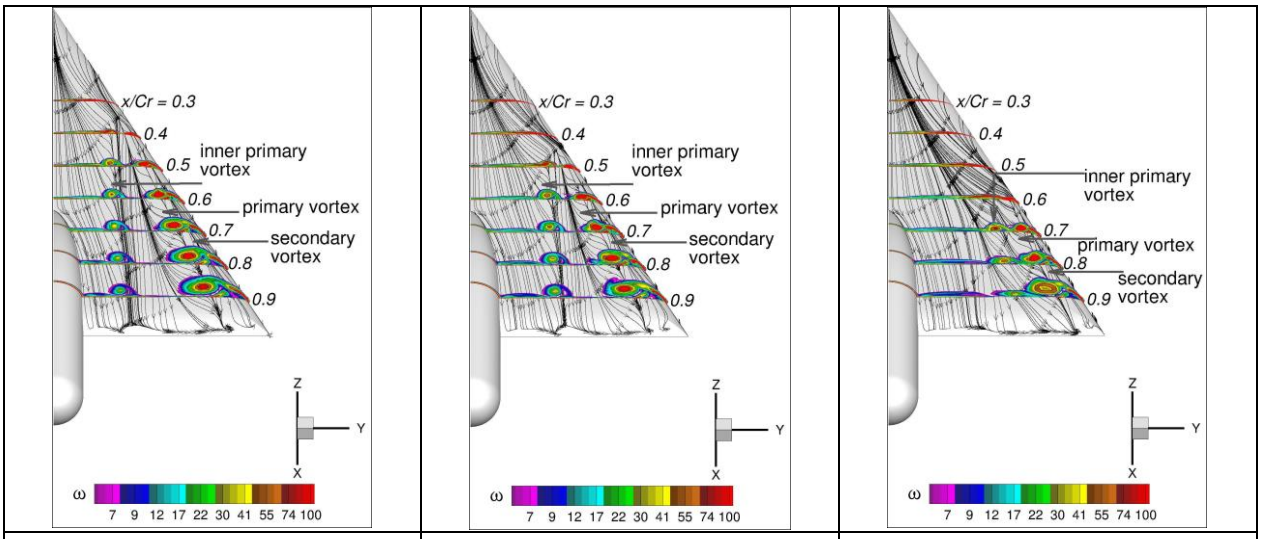

(a) Re = 2 million | (b) Re = 3 million | (c) Re = 6 million

Figure 17: Reynolds number study; Contours of vorticity and skin-friction lines.

To display the flow topology obtained at the different Reynolds numbers, skin-friction lines along with vorticity contours at different streamwise sections are shown in Figure 17. From the figure it is evident that the separation from the round leading edge and the formation of the inner and outer primary vortices move downstream with the Reynolds number. To illustrate the downstream movement of the flow separation, cp along the leading-edge of the delta wing at the different Reynolds numbers is shown. The line along which cp is extracted is shown in Figure 18(a) and the extracted cp-distributions are shown in Figure 18(b). At Re = 2 million, the decrease in cp shows attached flow extending up to the chordwise position of $x/c_r = 0.3$. Beyond this location the suction pressure collapses due to flow separation, according to [12]. With increasing Reynolds number the location where the suction pressure collapses moves downstream. This trend indicates downstream movement of flow separation and subsequent vortex formation.

The pressure coefficient distribution along the wing span at several streamwise locations is shown in Figure 19. In the figure, for visualization purpose, the cp distributions obtained at the Reynolds number of 3 million and 6 million are shifted by -2 and -4, respectively. At $x/c_r = 0.2$ in the experiments, attached flow can be observed with a suction peak located at the leading-edge for all the cases. This trend is reproduced in the numerical predictions. Further downstream of this location, at $x/c_r = 0.4$, still attached flow is evident for the higher Reynolds number cases in the experiments. However, for the Re = 2 million case, higher pressure at the leading-edge is observed due to separated flow. Local suction peaks (cp_{min}) at the spanwise location of $\eta = 0.5$ and 0.8 indicate the pressure associated with the outer primary and inner primary vortex cores. The outer primary vortex position and the associated pressure level, shown with a black arrow in Figure 19(b), are well reproduced in the numerical study. However, the inner primary vortex pressure, shown with a red arrow, is underestimated.

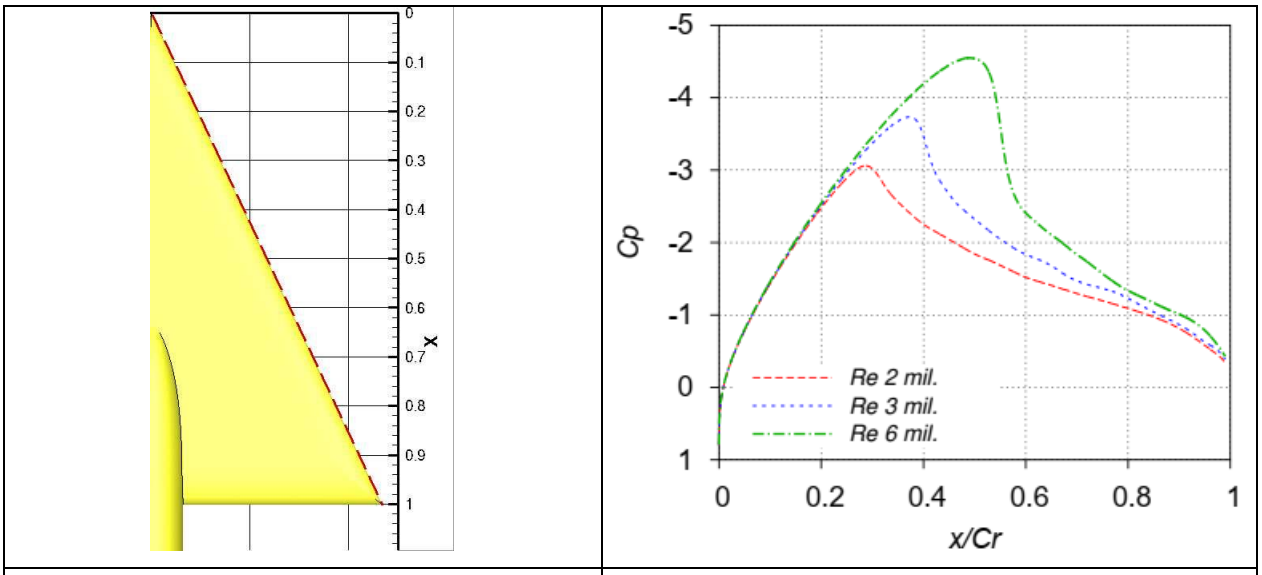

(a) Extracted cp line | (b) Cp at leading-edge

Figure 18: Pressure distribution along the leading edge of the delta wing at different Reynolds number.

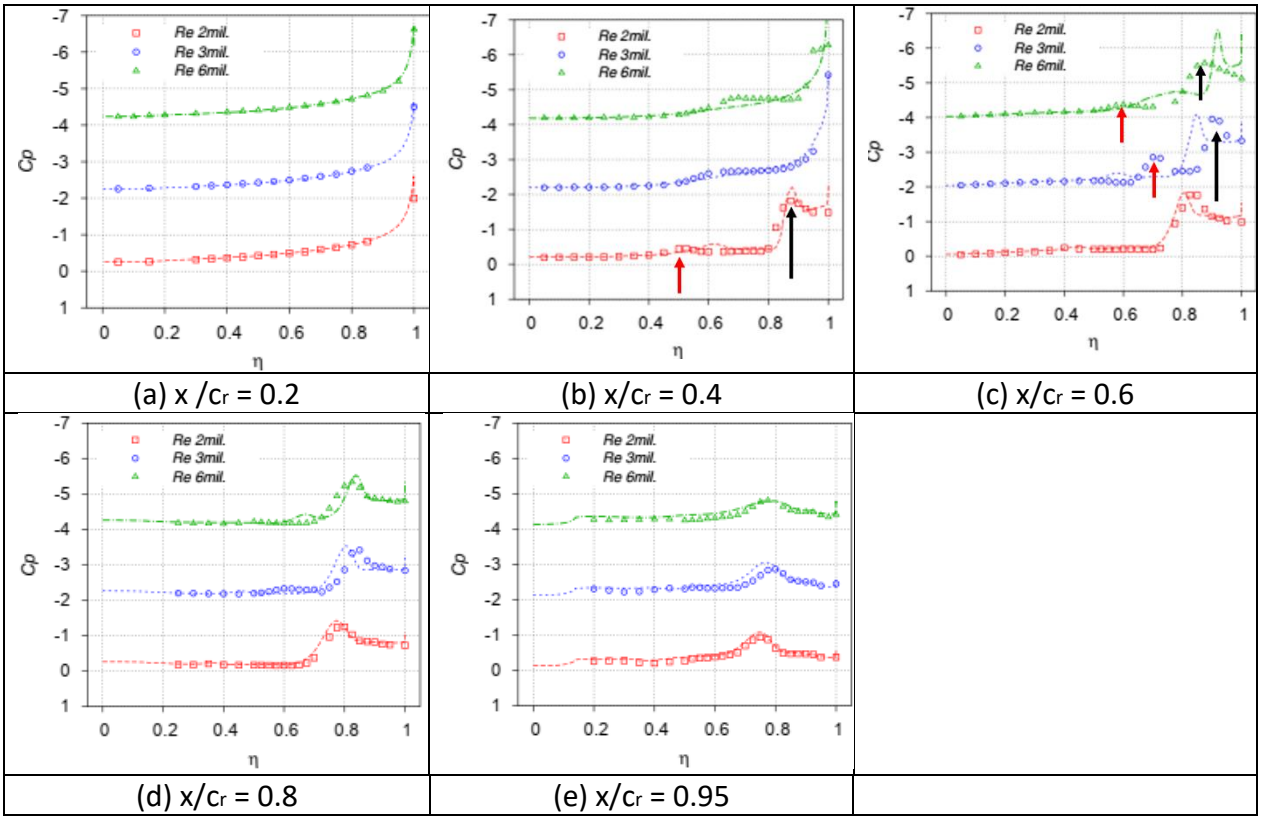

(a) x /c_r = 0.2 | (b) x/c_r = 0.4 | (c) x/c_r = 0.6

(d) x/c_r = 0.8 | (e) x/c_r = 0.95

Figure 19 Pressure distribution on the suction side of the delta wing for different Reynolds number at α = 13.3◦. Cp offset for successive Reynolds number case is 2.

At x/c_r = 0.6, in the experimental pressure distribution, a shift in the location of the suction pressure from the leading edge to the inboard section of the wing and local cp peaks unveil separated flow on the leading edge and inner and outer primary vortices (shown with arrows in

Figure 19(c). In the numerical investigations the same trend is observed. However, the location and the associated pressure distribution are underpredicted for the Re of 3 million and 6 million cases. Further downstream, at x/c_r = 0.8 and 0.95, an inboard movement of the outer primary vortex and lower cp peaks associated with the inner and outer primary vortices are evident from the experimental data. In the numerical investigation this trend and the pressure levels associated with the outer primary vortex are well reproduced.

Overall, for the case with Re of 2 million, the predictions agree well with the experimental data. For higher Reynolds number cases, major differences are observed at the streamwise station of 0.6. This can be due to an upstream position of the separation point delivered in the investigations compared to the experiments. At the other positions the predictions are in good agreement with the experimental data.

Diamond wing

The flow over a diamond wing at the incidence angle of 12° is investigated. Here, the objective is to assess how accurate a turbulence model can predict the incipient separation location and the pressure associated with the vortices which are formed as a result of flow separation.

Grid Refinement study

In the current work, the grid generation using the Centaur grid tool is not successful because of problems on the leading edge at the wing tip and as a result only the SOLAR grid generation tool is used. Here, three grids successively refined are generated. The grids have hexahedra cells in the near-wall region and tetrahedra cells in the remainder of the computational domain. The coarse grid has about 10 million grid nodes, while the medium and fine grids have 26 and 43 million nodes. An overview of the grid on the surface and in the farfield is shown in Figure 20(b). The grid refinement study is carried out on the three grid levels discussed earlier. Here the behavior of the results is assessed based on the variation of flow topology and the surface pressure distribution. With the RSM, a steady computation resulted in oscillatory force coefficients. As a result, time-accurate computations are carried out until the force coefficients converge.

Surface skin-friction lines along with the cp contours obtained on different grid levels are shown in Figure 12. On all grid levels, the foot prints of resolved vortex render the inner and outer primary vortices. On the medium and fine grids, a secondary vortex is also resolved whereas on the coarse grid it is not observed. Overall, on the medium and fine grids the flow topology looks almost the same. To display the flow separation from the blunt leading edge, cp along the leading edge is shown in Figure 22(a). The collapse of the suction peak renders the flow separation from leading edge. As can be seen, with the grid refinement the separation point moves upstream along the leading-edge. On the medium and fine grids only a slight change in the separation location with the grid refinement is observed.

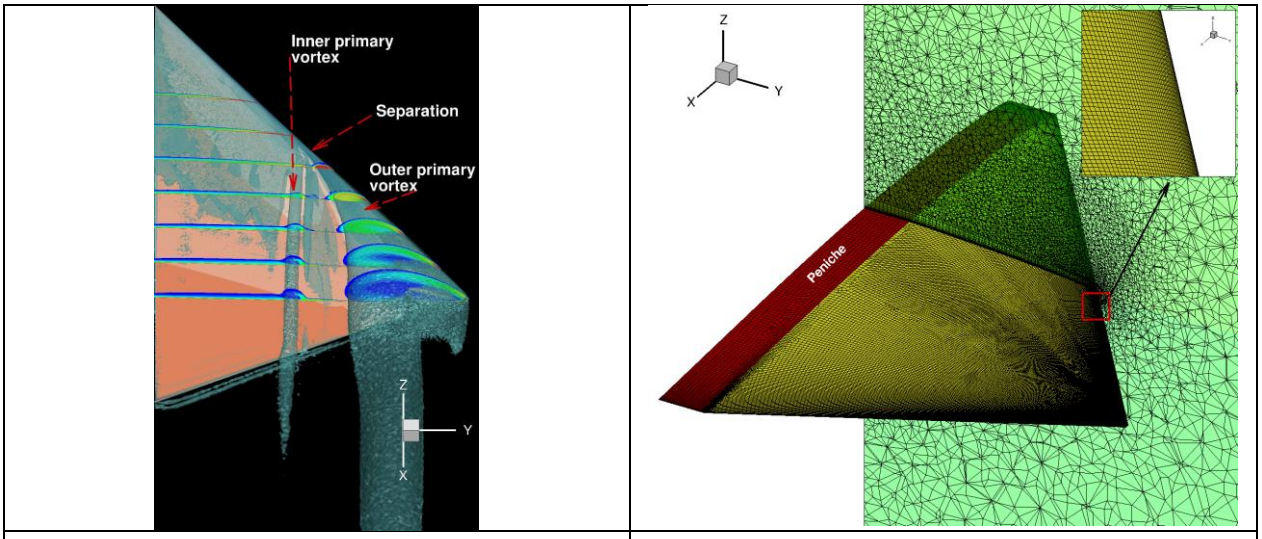

(a) Flow topology | (b) Grid (coarse)

Figure 20: Flow topology on the diamond wing at α = 12◦ and the computational grid on the surface and in the field.

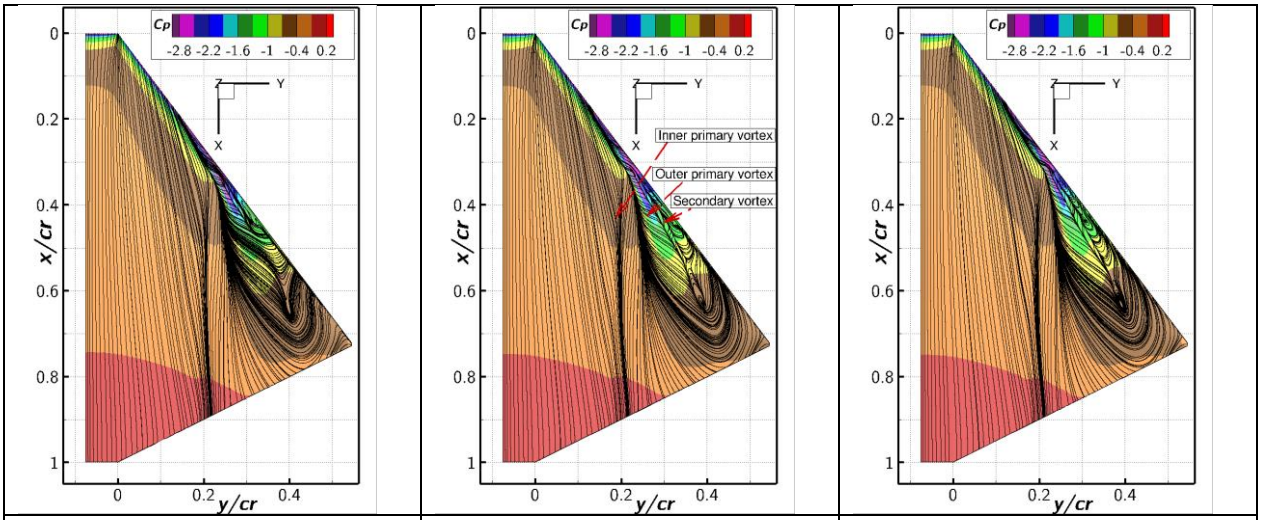

(c) Coarse | (d) Medium | (c) Fine

Figure 21: Contours of pressure coefficient delivered by RSM on different grids.

Sectional cp distributions obtained on the different grid levels are shown in Figure 22. At x/c_r = 0.1 and 0.2, due to attached flow almost identical pressure distributions are predicted on all grid levels. At x/c r = 0.3, on the medium and fine grids almost identical pressure is delivered. At x/c_r = 0.4, with increasing grid resolution higher pressure is predicted in the separated zone, y/s > 0.9. At x/c r = 0.5 and 0.6 almost identical pressure is delivered on the medium and fine grids. Overall, the grid refinement study unveils that the predictions do not change much on the medium and fine grids. For the further investigations, the fine grid is employed.

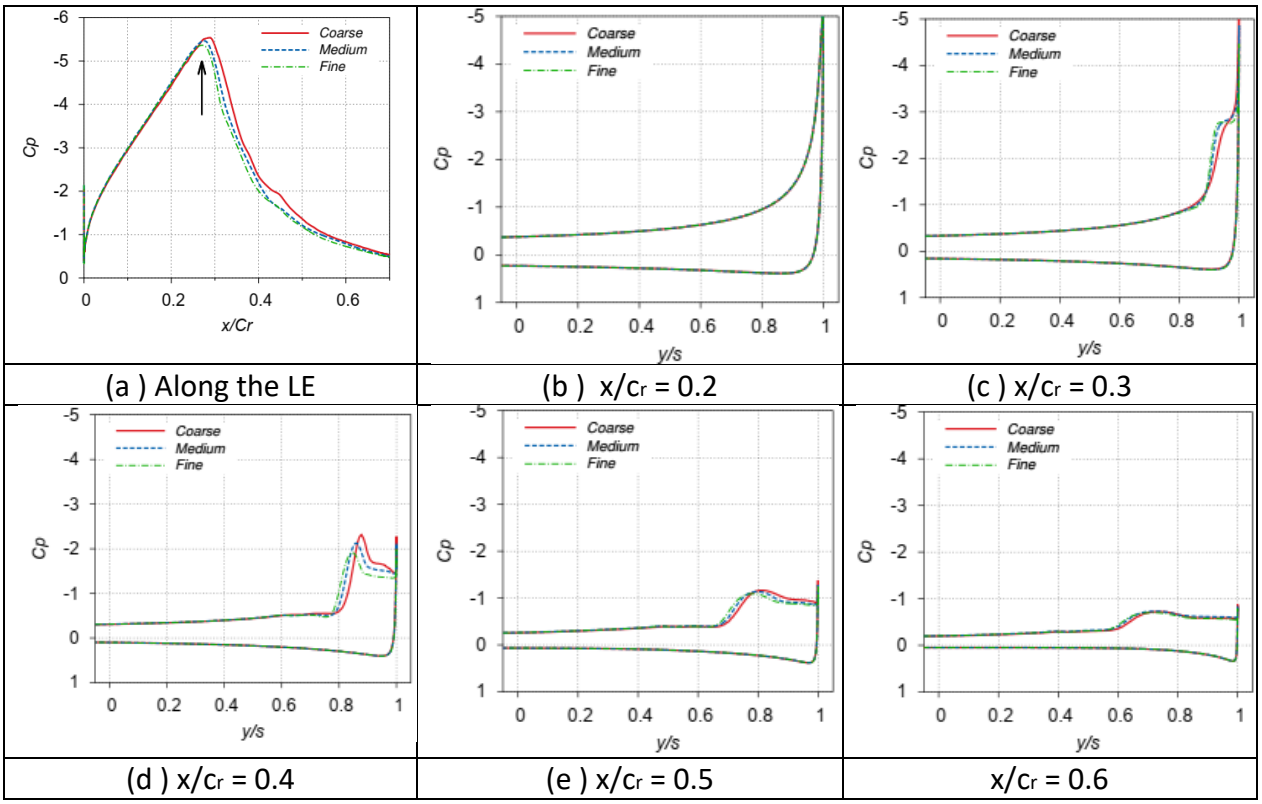

(a) Along the LE | (b) $x/c_r = 0.2$ | (c) $x/c_r = 0.3$

(d) $x/c_r = 0.4$ | (e) $x/c_r = 0.5$ | $x/c_r = 0.6$

Figure 22: Cp distribution delivered by RSM at different streamwise sections.

Turbulence model study

In this study, investigations are carried out with the SA-RC-QCR and RSM on the fine grid discussed in the previous chapter. The SA-RC-QCR computation converged in steady computation mode, whereas with the RSM time-accurate computations are required to flatten out the oscillations in the force coefficients observed in a steady computation. In Figure 23, the iso-surface of λ_2 and vorticity contours at several streamwise sections are shown. From the figure it is apparent that the SA-RC-QCR and RSM deliver both the inner and outer primary vortices. In the case of the SA-RC-QCR separation from the leading-edge occurs between the streamwise stations of 0.2 and 0.3 whereas in the cases of RSM, it occurs at x/c r = 0.3. Vorticity contours at x/c r = 0.6 display reduced levels of the vorticity magnitude in the SA-RC-QCR and RSM results compared to the upstream stations. The trend of reduced levels of vorticity magnitude is also observed in the experiments [8]. In the case of RSM the level of vorticity magnitude in the core is lower than in the SA-RC-QCR predictions. Low vorticity in the vortex core indicates the possibility of vortex breakdown.

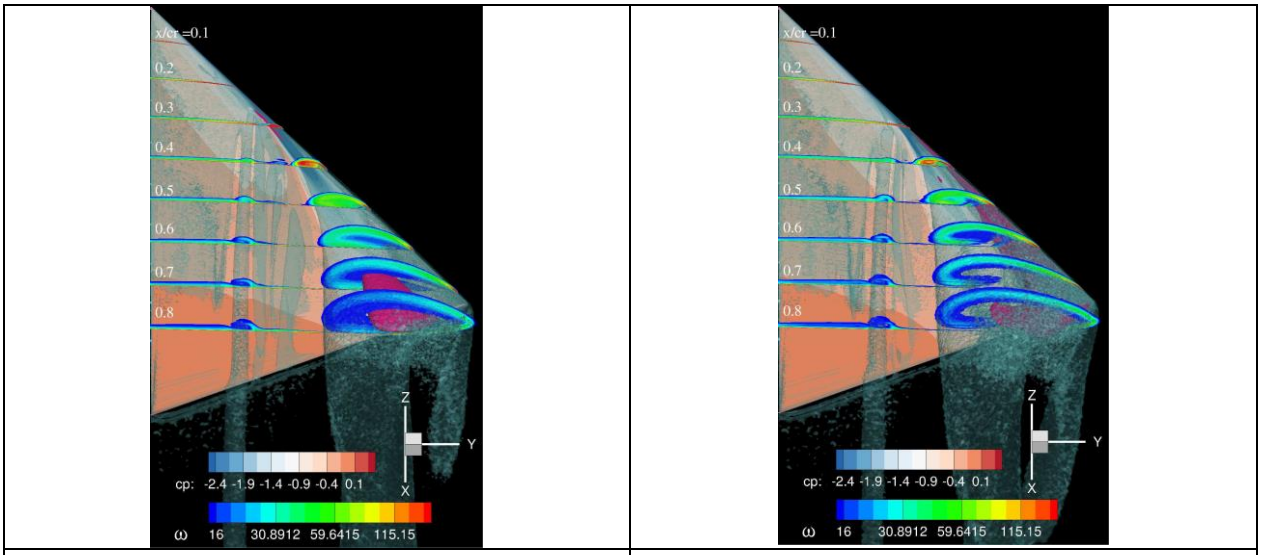

(a) SA-RC-QCR | (b) RSM

Figure 23: Iso-surface of λ_2 and the contours of vorticity magnitude on the fine grids.

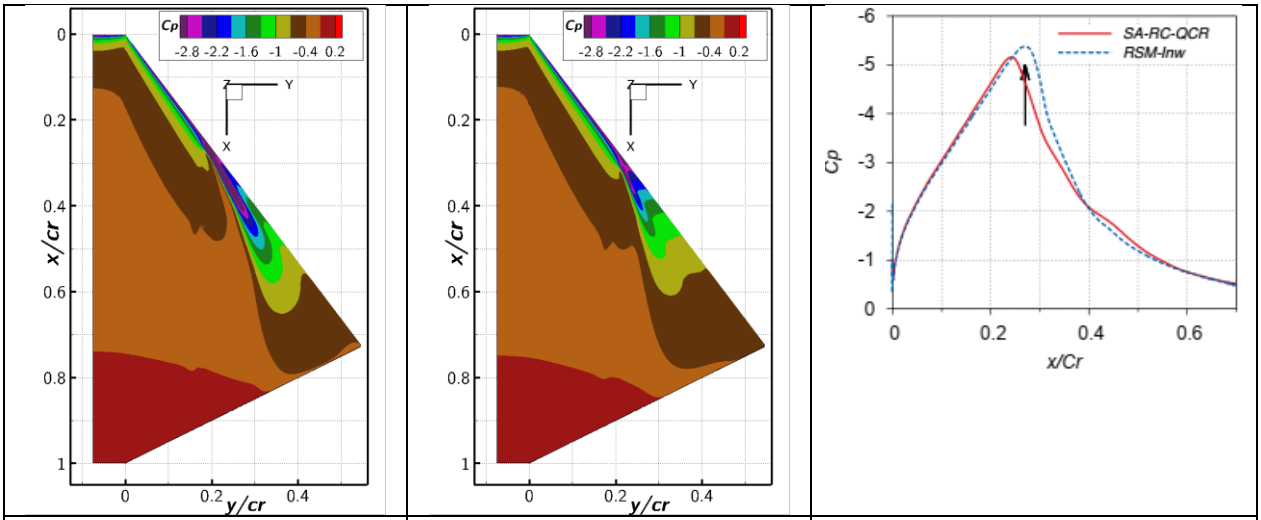

(a) SA-RC-QCR | (b) RSM | (c) cp along leading-edge

Figure 24: Cp contours on the diamond wing and Cp along the leading edge.

Pressure coefficient distributions delivered by the SA-RC-QCR and RSM are shown in Figure 24. In the case of SA-RC-QCR a shift in the location of suction pressure from the leading edge to the inboard section of the wing, indicating flow separation, is observed upstream of $x/c_r = 0.3$ whereas in the case of RSM this region is observed directly at $x/c_r = 0.3$.

The cp along the wing leading edge is shown in Figure 24(c). The decrease of the suction pressure indicates the region close to flow separation. As can be seen in the SA-RC-QCR the flow separation from round leading edge occurs earlier than in the RSM. In the pressure contour plots, the extent of suction pressure associated with the outer primary vortex is smaller in the

case of RSM compared to the SA-RC-QCR. This is due to the enlarged vortex in the inboard direction and reduced vortex strength in the RSM predictions.

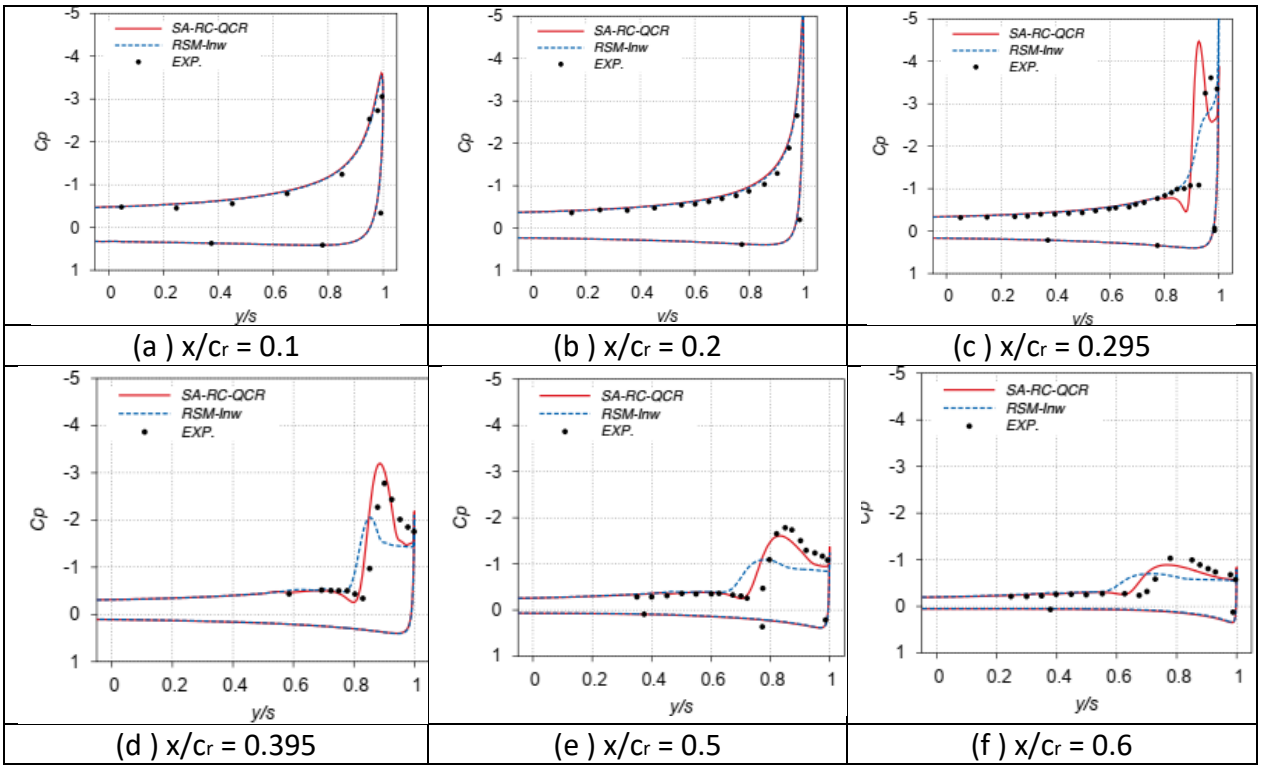

Figure 25: Comparison of Cp distribution on fine grid for the delta wing.

Figure 25 shows the comparison of predicted cp with the experimental data. At the streamwise stations of x/c_r = 0.1 and 0.2 the experimental pressure distributions render attached flow. This trend is reproduced in the computations and the predicted pressure is in good agreement with the experiments. At x/c r = 0.295, the experimental cp displays vortex separation by a shift of the suction peak from the leading edge to an inboard location of the wing. In the SA-RC-QCR computation, due to earlier separation, the outer primary vortex is located too far inboard with a higher suction peak compared to the experiments. In the cases of RSM the cp distribution renders attached flow, however a rather slow change in the cp gradient displays that the flow is on the verge of separation.

At further downstream locations, x/c r = 0.395 to 0.6, a fully developed separated vortex flow trend is observed in the experiments. The local cp peak represents the pressure associated with the vortex. As can be seen in the figure, the pressure associated with the outer primary vortex and its location are well reproduced in the SA-RC-QCR predictions. However, in the RSM investigations, the suction peak associated with the outer primary vortex is underpredicted and its location is delivered more inboard compared to the experiments.

Overall, for this test case, the SA-RC-QCR shows good agreement with experiments with respect to the pressure associated with the outer primary vortex and its location despite earlier

separation. Concerning the RSM, though closer agreement with experimental separation location, the downstream development of the vortex is underpredicted.

Discussion on the performance of RANS models

All the configurations investigated unveil separation from smooth body surface and subsequent formation of vortices. For the spheroid configuration, all the applied RANS models exhibited similar performance—all the models delivered vortices with almost the same strength, which is weaker compared to experiments. For this configuration, RSM has not displayed many improvements compared to the other turbulence models.

For the delta and diamond wing investigations, SST-RC-QCR is not considered for the investigations as it predicts flow separation much too early. For the delta wing, RSM demonstrated improvements with respect to the locations of vortex separation from leading edge and inner primary vortex, which are closer to the experiments.

For the diamond wing, RSM performs poorly by delivering weaker outer primary vortex compared to experiments. For this case, in spite of earlier flow separation, the SA-RC-QCR delivered improved predictions with respect to the downstream development of outer primary vortex.

Assessment of hybrid RANS/LES based on eddy viscosity models

Here, the DDES based on SA and SA-RC-QCR are employed to assess the capabilities of standard hybrid RANS/LES methods for vortex separated flows. As the objective is to evaluate the potential advantages over RSM models for these flows, the DDES predictions are compared to RSM predictions and the experimental data. In this study the flow over delta wing and diamond wing at moderate incidence angle, mentioned in the previous sections, where partially separated flow prevail are investigated. It should be noted that the partially separated flows pose challenges to DDES as the flow separation stays very close to near wall regions where the hybrid model is neither fully in RANS mode, nor yet fully in LES mode. In this investigation, the advantages of applying DDES for the vortex separated flows is examined with respect to improvement of separation location and vortex strength.

In the DDES studies, the RANS results discussed earlier are used as an initial solution and advancement in time is carried out with a non-dimensional time step size of 0.001. Initially, the flow is let to develop over 4 to 5 convective time units and then time-averaging of the flow is carried out until time-averaged force coefficients settle down. In the current investigations, the time-averaging is carried out for about 10 CTUs. The grids used for the current investigation are the fine grids from the grid refinement study discussed earlier. For the delta wing the grid has about 44 million grid nodes and the diamond wing grid has about 43 million nodes.

Delta wing

To unveil the instantaneous flow topology delivered by RSM, SA-DDES and SA-RC-QCR-DDES the iso-surface of λ_2 and the vorticity magnitude contours at different streamwise sections are depicted in Figure 26. With the RSM, flow separation occurs at $x/c_r = 0.4$ and forms the outer

primary vortex. According to [1], a part of the flow from the outer primary vortex moves towards the inboard section of the wing after reattachment and its interaction with the attached flow from the apex leads to the inner primary vortex which is delivered with the RSM. In the case of SA-DDES flow separation occurs at about $x/c_r = 0.48$ and forms the inner primary and outer primary vortices. However, in contrast to the RSM results and the experiments, the inner primary vortex merges with the outer primary vortex a short distance downstream of the vortex separation. With the SA-RC-QCR-DDES flow separation is predicted at $x/c_r = 0.3$ which is upstream of the separation observed with the SA-DDES and RSM, see Figure 26(c). Concerning the inner and outer primary vortices, the SA-RC-QCR-DDES predicts both vortices. In both DDES investigations parallel vortices aligned with the flow direction are resolved on the inboard section of the wing. In the experimental investigations the existence of parallel aligned vortices on the inboard section of the wing has not been discussed.

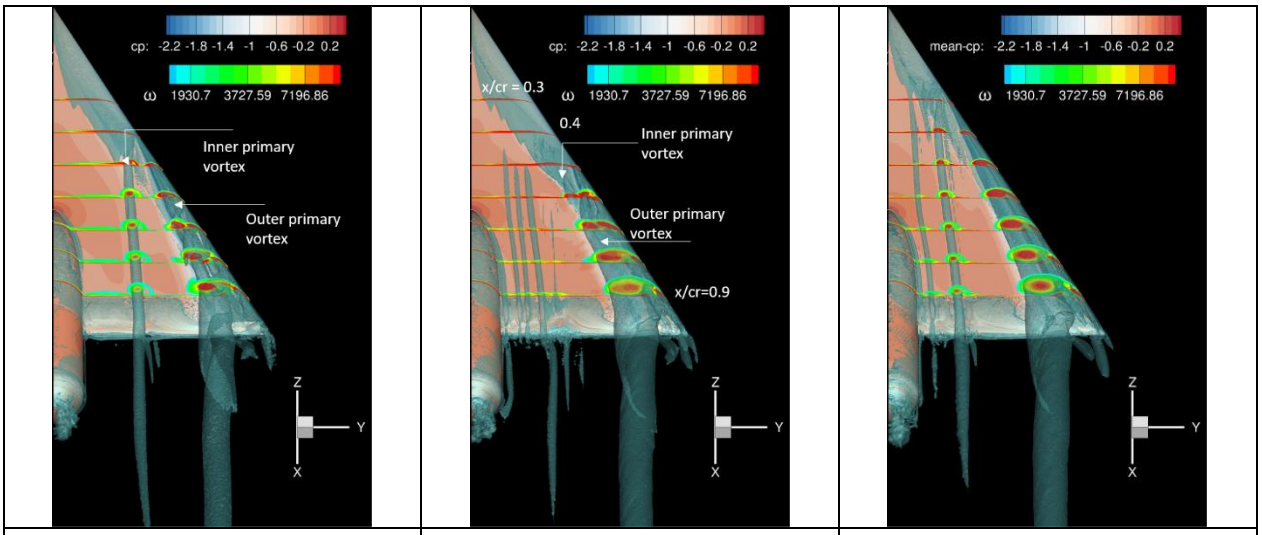

(a) RSM	(b) SA-DDES	(c) SA-RC-QCR-DDES

Figure 26: Contours of vorticity magnitude and the iso surface of λ_2 of the time-averaged flow field on the delta wing.

Figure 27 presents the surface pressure distribution on the suction side of the wing from the experiments and the predictions delivered by the RSM and DDES computations. In the experiments the movement of the suction pressure from the leading edge to the inboard section of the wing indicates flow separation and subsequent formation of an outer primary vortex, see Figure 27(a). From the contours of the experiments, it is apparent that the separation occurs at $x/c_r = 0.48$. In the figure the suction pressure associated with the outer primary vortex is depicted with a blue streak. A bit inboard from the outer primary vortex another local cp_{min} streak in the experiment illustrates an inner primary vortex.

In the RSM predictions the flow separates from the leading edge at about $x/c_r = 0.4$, and inner and outer primary vortices can be observed. The inner primary vortex is located slightly inboard in the RSM results compared to the experiments as the separation is predicted earlier than in the experiments. Concerning the pressure associated with the outer primary vortex, the cp level

delivered in the RSM predictions agrees with the experiments, however, its position is located slightly inboard.

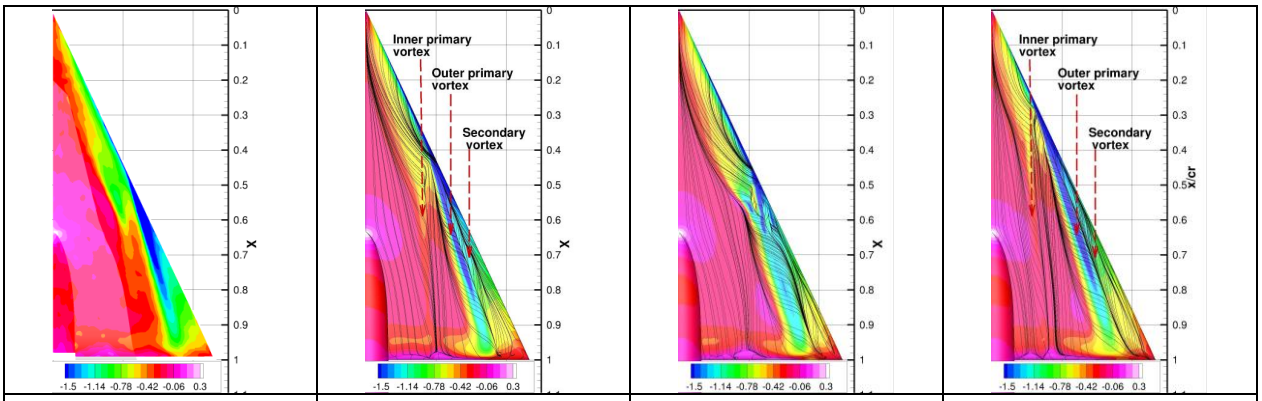

(a) Exp. | (b) RSM | (c) SA-DDES | (d) SA-RC-QCR-DDES

Figure 27: Contours of pressure coefficient and skin-friction lines on the delta wing.

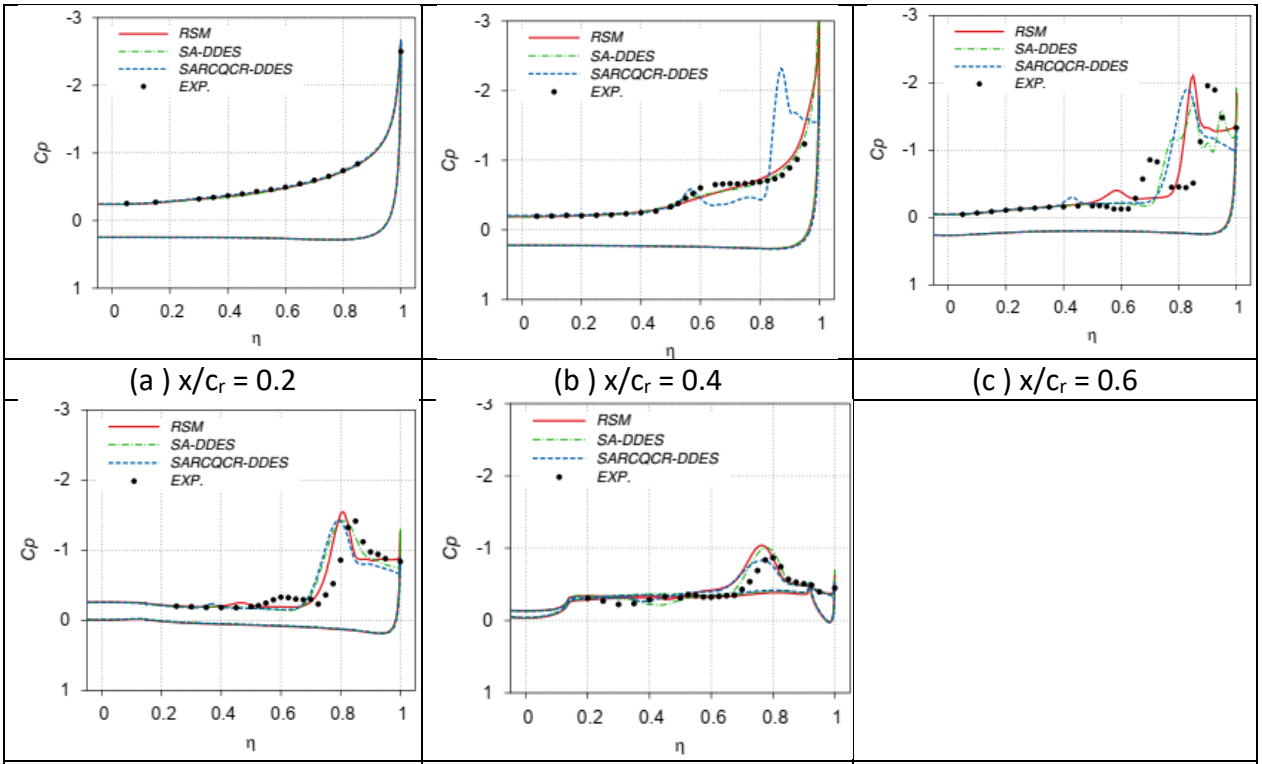

(a) x/c_r = 0.2 | (b) x/c_r = 0.4 | (c) x/c_r = 0.6

(d) x/c_r = 0.8 | (e) x/c_r = 0.95

Figure 28: Sectional cp distribution on the delta wing.

In the SA-DDES predictions, the flow separates at about x/c_r = 0.48 and forms the outer primary vortex, see Figure 27(c). The pressure associated with the vortex is higher than in the experiments. Furthermore, the inner primary vortex is not predicted. In the SA-RC-QCR-DDES predictions the flow separates from the leading edge at about x/c_r = 0.3 and forms both the inner and outer primary vortices, see Figure 27(d). The location of flow separation is predicted

too far upstream compared to the experiments and the RSM predictions. This upstream movement of separation resulted in a more inboard located inner primary vortex. In spite of the more inboard located vortices, the suction pressure associated with the outer vortex is closer to the experiments.

The comparison of the sectional pressure distribution is shown in Figure *28*. At the streamwise station of $x/c_r = 0.2$, attached flow pressure distribution is observed in the experiments. This trend is reproduced in all the predictions. At $x/c_r = 0.4$, see Figure 28(b), the suction peak is located at the leading edge which unveils attached flow in the experiments. In addition to this the experimental cp shows a plateau on the inboard section which indicates the flow on the verge of separation. In the RSM and SA-DDES predictions attached flow trend is delivered. Both models failed to deliver cp plateau on the inboard section of wing. In SA-RC-QCR-DDES the suction peak is located inboard which indicates earlier vortex separation. And the two suction peaks at $\eta = 0.86$ and 0.58 unveil the locations of the outer primary vortex and the inner primary vortex, respectively. At this location the predictions of SA-RC-QCR-DDES do not show the experimental trends.

At $x/c_r = 0.6$, the experiments show a vortex separation trend and unveil two suction peaks which render the pressure associated with the inner and outer primary vortices and their locations. In the experiments the outer primary vortex is located at η of about 0.9 and the inner primary vortex is located at η of about 0.7. As can be seen in the Figure 28(c), all the models predict the outer primary vortex more inboard compared to the experiments. In the RSM-ln(ω) and SA-RC-QCR-DDES predictions the suction peak level associated with the outer primary vortex agrees with the experiments. In the SA-DDES predictions the lower suction peak of the outer primary vortex is because of the weaker vortex compared to the other predictions and experiments.

The suction pressure of the inner primary vortex is underpredicted in the RSM and SA-RC-QCR-DDES results which indicate that the strength of the inner primary vortex in the predictions is considerably weaker than in the experiments. Concerning the location of the inner primary vortex, both modeling approaches deliver the inner primary vortex more inboard compared to the experiments. The reason for the more inboard located inner primary vortex is the more upstream prediction of flow separation compared to the experiments. In the SA-DDES predictions the suction pressure associated with the inner primary vortex is not observed as it fails to capture the vortex on this grid. Farther downstream at $x/c_r = 0.8$ and 0.95, more inboard located inner and outer primary vortices compared to experiments are delivered by RSM and a weaker inner primary vortex compared to experiments is computed by SA-RC-QCR-DDES.

Discussion on the capabilities of EVM based SRS for the delta wing

For the delta wing considered in the present study, the experimental data unveil flow separation midway along the leading edge and the presence of outer and inner primary vortices. The SA-DDES delivers the experimental vortex separation location and predicts the inner primary and outer primary vortices. However, in contrast to the experiments, a short

distance after the inception of the inner primary vortex, fusion of the inner primary and outer primary vortices is observed. Additionally, the strength of the outer primary vortex is predicted too weak compared to experiments.

When the SA-DDES is coupled with the rotational correction and quadratic constitutive relation, it predicted separation too far upstream of experimental separation location. This leads to more inboard located inner and outer primary vortices. These additional extensions have not improved the prediction of the strength of vortices. A possible reason for the upstream movement of separation location is the rotation/curvature correction term which is usually active on the leading-edge region that reduces turbulence level in the boundary layer that may have led to earlier separation.

For partially separated flows, such as these, the accurate prediction of vortex separation is decisive for the downstream development of the vortex. In the RANS performance study, it is observed that the use of the rotational correction and quadratic constitutive relation extensions with the SA lead to more upstream movement of separation location compared to the experiments. In the present study, the same trend is observed in the SA-RC-QCR-DDES investigations as the SA-RC-QCR turbulence model is employed in the near wall region. From this study, it seems the use of additional extensions may not be necessary for the prediction of these partially separated flows.

On the given grids and based on the solver settings applied for this configuration, the RSM shows the tendency to represent the flow slightly better than the DDES by delivering separation locations closer to experiments and stronger outer and inner primary vortices compared to the other methods employed.

Diamond wing

Figure 29 shows the iso-surface of λ_2 along with vorticity contours of the time-averaged flow field. As can be seen in the RSM predictions the flow separation and subsequent vortex formation occurs about $x/c_r = 0.3$ while in SA-DDES it occurs at about $x/c_r = 0.35$ which agrees with the experimental finding. In the case of SA-RC-QCR-DDES the vortex separation occurs at $x/c_r = 0.25$ which is far too upstream of the trend observed in the SA-DDES. On the inboard section of the wing, an additional weak inner primary vortex is predicted in the RSM predictions. A similar trend is also delivered in both variants of DDES investigations.

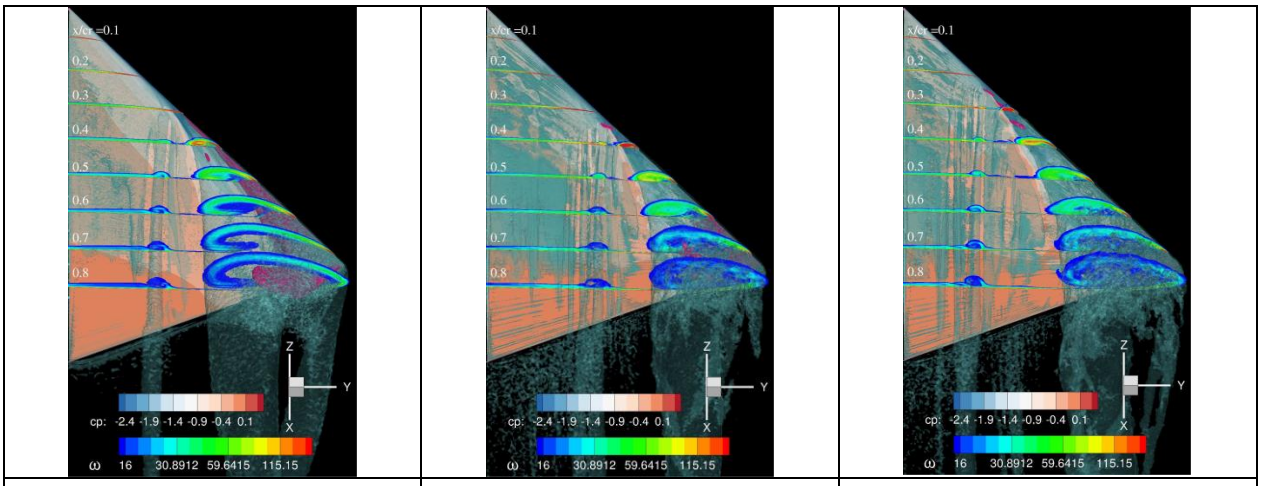

(a) RSM | (b) SA-DDES | (c) SA-RC-QCR-DDES

Figure 29: Contours of the vorticity magnitude and iso-surface of λ_2 of the time-averaged flow field for the diamond wing.

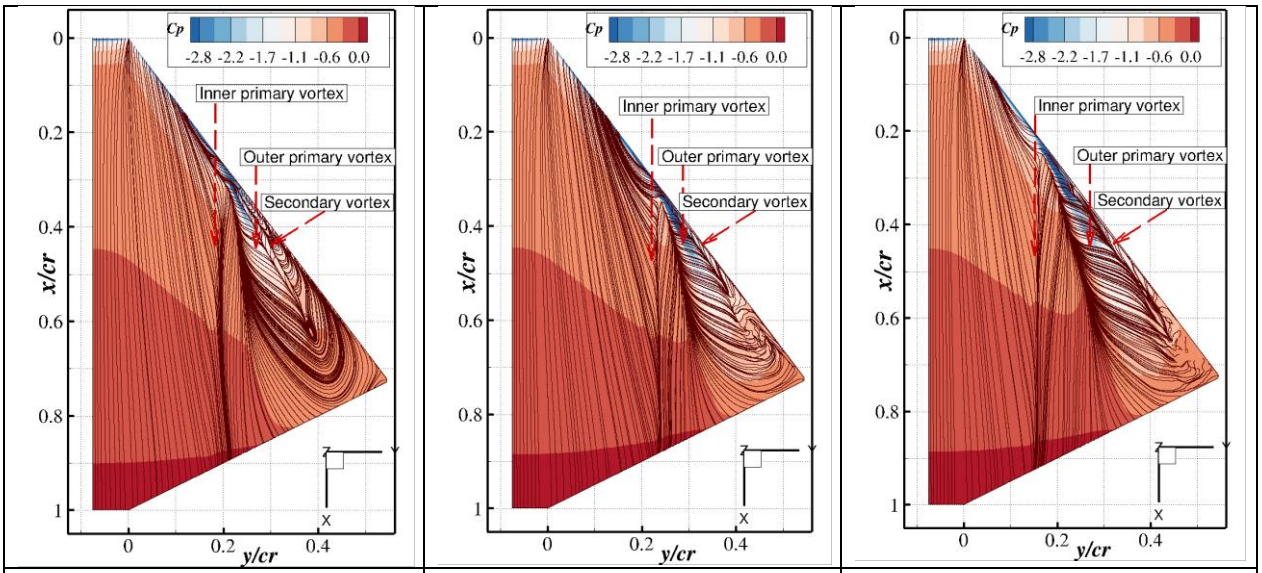

(a) RSM | (b) SA-DDES | (c) SA-RC-QCR-DDES

Figure 30: Contours of pressure coefficient and skin-friction lines.

In Figure 30 the surface pressure distribution along with the skin-friction lines are shown. As is visible from the figures, the foot prints unveil the predicted inner primary and outer primary vortices yielded by all the models. In the case of SA-RC-QCR-DDES the inner primary vortex is located more inboard compared to the other two predictions. In the RSM predictions the location of the inner primary vortex is a bit outboard compared to the SA-RC-QCR-DDES and inboard compared to the SA-DDES. Apparently, the position of the inner primary vortex depends on the vortex separation location. The earlier the vortex separation the more inboard located is the inner primary vortex.

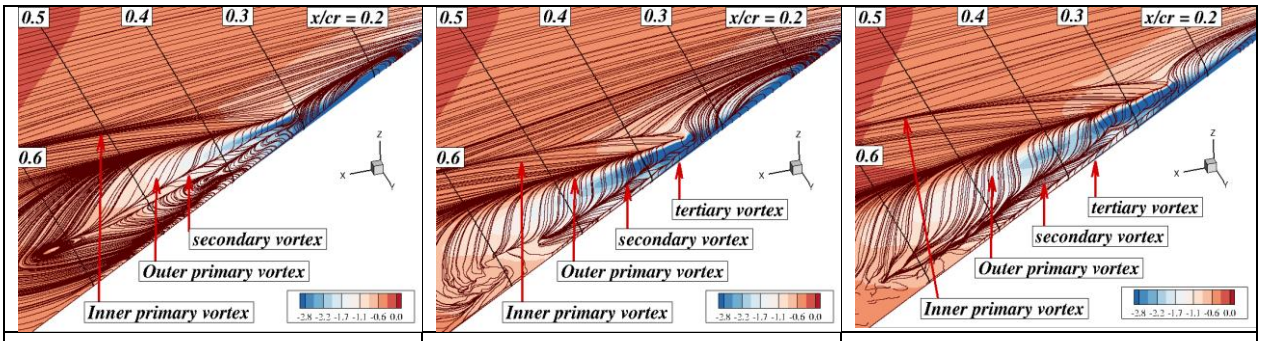

(a) RSM	(b) SA-DDES	(c) SA-RC-QCR-DDES

Figure 31:Close-up view of leading edge with the contours of pressure coefficient and skin-friction lines.

To visualize further the predicted vortices, a close-up view of the leading-edge region is shown in Figure 31. In the SA-DDES and SA-RC-QCR-DDES cases secondary and tertiary vortices are predicted. In the case of RSM, in addition to these vortices, a whirl can be observed where the outer primary vortex collapses with the secondary vortex.

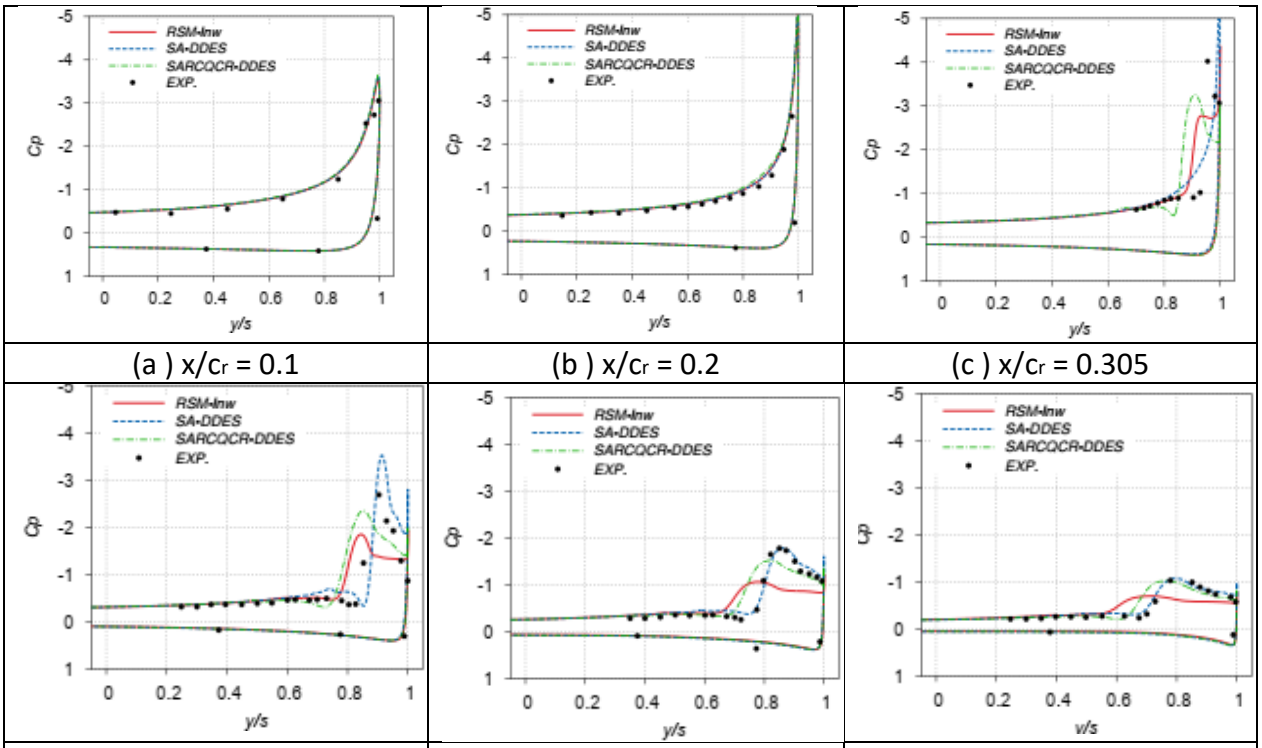

(a) x/c_r = 0.1	(b) x/c_r = 0.2	(c) x/c_r = 0.305
(d) x/c_r = 0.405	(e) x/c_r = 0.5	(f) x/c_r = 0.6

Figure 32: Cp distribution at different streamwise sections.

The comparison of the sectional pressure distribution is displayed in Figure 32. At the streamwise sections of x/c_r = 0.1 and x/c_r = 0.2 the experiments show the trend of an attached flow. This trend is reproduced in the predictions with all the turbulence models applied. At x/c_r = 0.305, in the experiments the inboard movement of the suction peak from the leading edge

indicates flow separation and subsequent vortex formation. The location of the suction peak also indicates the vortex axis. As can be seen in Figure 32, the SA-DDES predicts attached flow at this location while SA-RC-QCR-DDES delivers the experimental trend, however, the predicted vortex axis is more inboard compared to the experiments which is because of the earlier vortex separation than in the experiments. In the RSM prediction, the flow is still attached with the suction peak at the leading edge. A plateau in cp on the inboard leading edge indicates the flow is on the verge of separation in the RSM.

At $x/c_r = 0.405$, in the experiments a lower suction peak compared to the previous location is observed. This is because with the downstream distance the size of the vortex grows and its strength decreases. The location of cp_{min} indicates that the vortex core axis moves inboard with the downstream distance. At this streamwise station the predictions of the SA-DDES are in good agreement with experimental data with regard to the vortex position and the cp level associated with it. The SA-RC-QCR-DDES predicts the vortex more inboard and delivers lower cp compared to the experiments as a weaker vortex is predicted. In RSM the position of the vortex is predicted more inboard and delivers lower cp compared to the experiments. From the contours of the vorticity magnitude, see Figure 23, and the cp level it is apparent that the predicted vortex in RSM is the weakest. At farther downstream locations the vortex core axis and the cp levels are well predicted by the SA-DDES. Both the SA-RC-QCR-DDES and RSM deliver the vortex more inboard and lower cp compared to the experiments.

Though the SA-DDES predicts the vortex separation slightly downstream of the experimental location, it delivers the cp associated with the vortex and its position much better than the other turbulence model predictions.
Overall, for this test case the SA-DDES performs better than the other modeling approaches applied.

Assessment of hybrid RANS/LES based on a Reynolds-stress model

In this section investigations carried out with the DDES based on RSM are discussed. To assess the performance of the RSM-DDES, the predictions obtained for different configurations are compared to the experimental data and predictions of RSM and SARCQR-DDES.

Delta wing

The global feature of the flow is unveiled in Figure 33 by showing the iso-surface of λ_2 along with the contours of vorticity magnitude of the time-averaged flow field. In the figure, streamwise sections are located from $x/c_r = 0.3$ to 0.9 with a distance between each station of 0.1. In all the predictions, both the outer primary and inner primary vortices are delivered. In RSM-DDES and SA-RC-QCR-DDES predictions, flow separation from leading edge and formation of outer primary and inner primary vortices occur upstream of $x/c_r = 0.3$, which is earlier than in the RSM predictions. In cases of RSM-DDES and SA-RC-QCR-DDES, one more streamwise vortex aligned with the freestream is resolved. As it can be seen in the figure the streamwise extent of this vortex is longer in SA-RC-QCR-DDES compared to RSM-DDES.

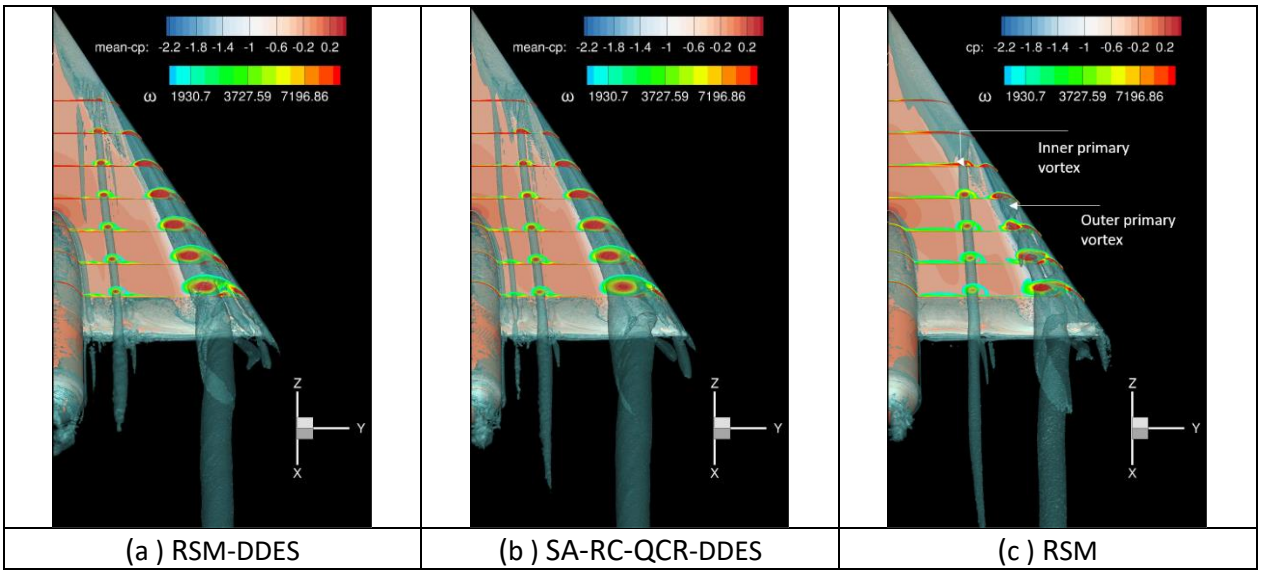

(a) RSM-DDES | (b) SA-RC-QCR-DDES | (c) RSM

Figure 33: Contours of vorticity magnitude and the iso surface of λ_2 on delta wing of the time-averaged flow field.

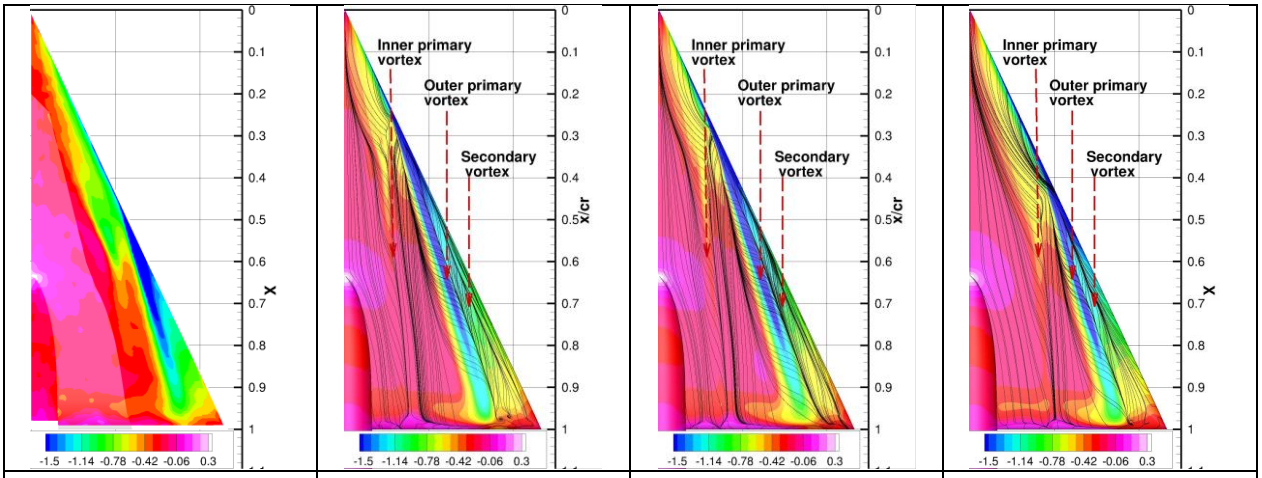

(a) Exp. | (b) RSM-DDES | (c) SA-RC-QCR-DDES | (d) RSM

Figure 34: Contours of pressure coefficient and skin-friction lines of time-averaged field on the delta wing.

Contours of surface pressure distribution delivered by different models is shown in Figure 34 and compared with the experimental data. Additionally, the surface skin-friction lines in the numerical investigations are shown to render the vortex footprint. In the experiments, the movement of suction pressure from the leading edge towards the inboard section indicates the flow separation and formation of the outer primary vortex. In the experiments, based on the cp distribution, flow separation appears to occur at the streamwise station of $x/c_r = 0.48$. In the predictions, this trend is observed more upstream than in the experiments.

A bit inboard from the separation point in the experiments, a local cp minimum in the region, shown with green color, render the origin of the inner primary vortex and associated pressure

with it. In the predictions, the location is observed to be more inboard and the pressure associated with the vortex is higher compared to the experiments. The reason for the more inboard located inner primary vortex is the more upstream flow separation in predictions.

In all the DDES investigations, earlier flow separation is predicted compared to the experiments. Among all the predictions, the separation location delivered by the RSM is in closer agreement with the experiments.

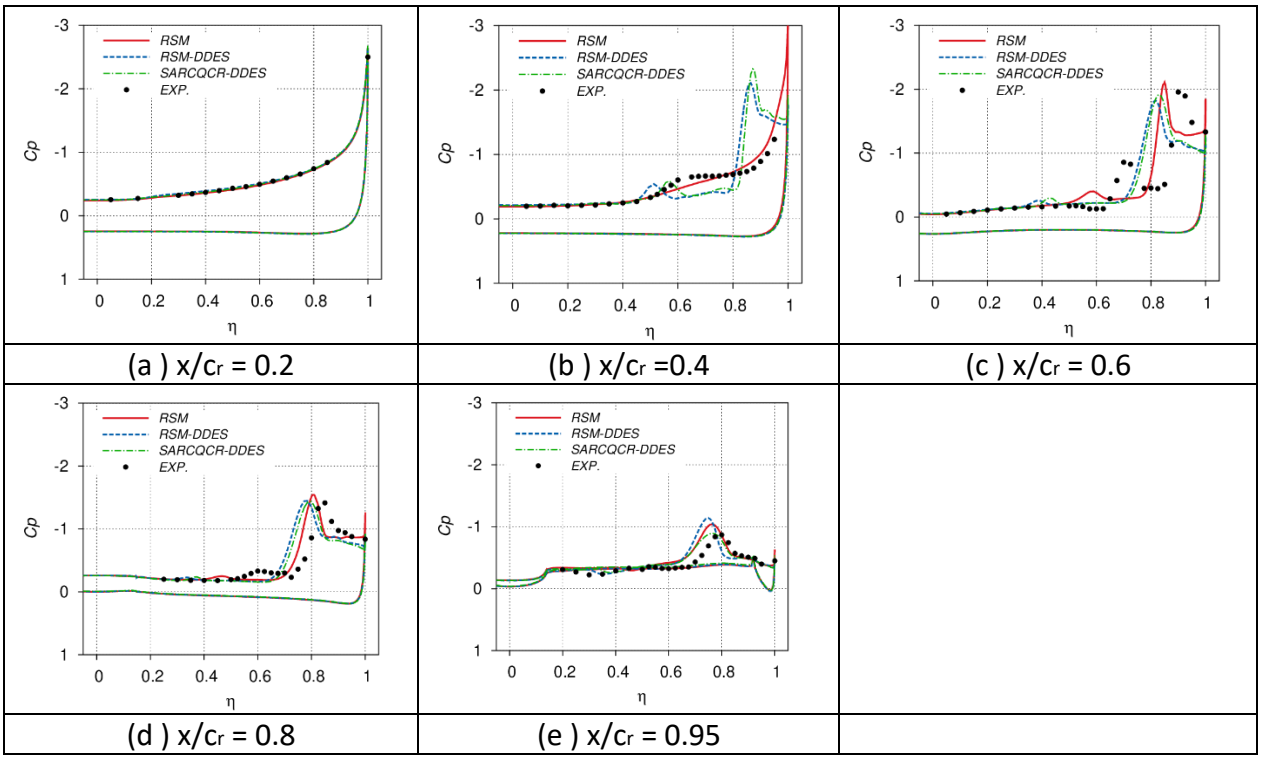

(a) x/c_r = 0.2 | (b) x/c_r =0.4 | (c) x/c_r = 0.6

(d) x/c_r = 0.8 | (e) x/c_r = 0.95

Figure 35: Sectional cp distribution on delta wing.

In Figure 35, the sectional pressure distribution from the simulations is compared to the experimental data. At the streamwise section x/c_r = 0.2, attached flow is observed in the experiments. A similar trend is delivered in all the predictions. Downstream of the aforementioned location at x/c_r = 0.4, the experimental pressure distribution still shows attached flow trend. A plateau in cp distribution indicates the flow on the verge of separation. In contrast to the experiments, in both scale-resolving predictions, loss of suction peak at the leading edge is delivered due to flow separation and subsequently local suction peaks at spanwise location η of 0.85 and 0.6 caused by the formation of outer primary vortex and inner primary vortex, respectively. With RSM, similar to the experiments, attached flow is observed at this streamwise location.

At x/c_r = 0.6, the experimental pressure distribution shows the presence of outer and inner-primary vortices with the suction peaks at spanwise location η of 0.9 and 0.7, respectively. At this location, all the predictions reproduce the experimental trend. However, the locations of

both vortices are delivered more inboard due to earlier flow separation compared to the experiments. Concerning the vortex strength, shown with the level of suction peak, all DDES simulations delivered weaker outer primary vortex and this resulted in lower suction peak associated with the vortex. For the inner primary vortex, much weaker vortex compared to the experiments is predicted in all the predictions. In RSM predictions, since the vortex flow separation is closer to the experiments, the suction peak associated with the outer primary vortex agrees well with the experiments. However, the suction peak of the inner primary vortex is underpredicted.

At further downstream locations, lower suction peaks for the inner and outer primary vortices compared to the upstream sections are observed in the experiments. This trend is reproduced in all the predictions. However, the vortices are located more inboard compared to the experiments.

The applied SA-RC-QCR-DDES and RSM-DDES approaches on the grids employed in this study do not show any improvement in the predictions compared to the unsteady RSM for this configuration.

The DDES with SA-RC-QCR and RSM deliver earlier flow separation from the round leading edge which leads to earlier formation of outer and inner primary vortices compared to the experiments, while the unsteady RSM predicted flow separation closer to the experimental separation location. The upstream movement of the separation location in SA-RC-QCR-DDES is attributed to the underlying RANS turbulence model, SA-RC-QCR. In RSM-DDES, earlier flow separation is caused by the modelled-stress-depletion [15], more details in the discussion section.

Diamond wing

An iso surface of λ_2 and slices with the vorticity magnitude of the time average flow field are shown in Figure 36. As it can be seen in the figure, flow separation from the leading edge and subsequent formation of outer primary vortex occurs at about $x/c_r = 0.2$ in RSM-DDES. In the case of SA-RC-QCR-DDES, flow separation occurs at $x/c_r = 0.25$. In contract, in RSM flow separation is predicted at $x/c_r = 0.3$, which is the most downstream location compared to the other predictions. In the experiments, vortex separation at is observed upstream of $x/c_r = 0.3$. In all the predictions, the outer primary vortex and a weak inner primary vortex is predicted, which agrees with the experimental trend. In the predictions of RSM-DDES and SA-RC-QCR-DDES, additional streamwise vortices parallel to inner primary vortex are resolved. A trend that is also observed of the delta wing with scale-resolving methods.

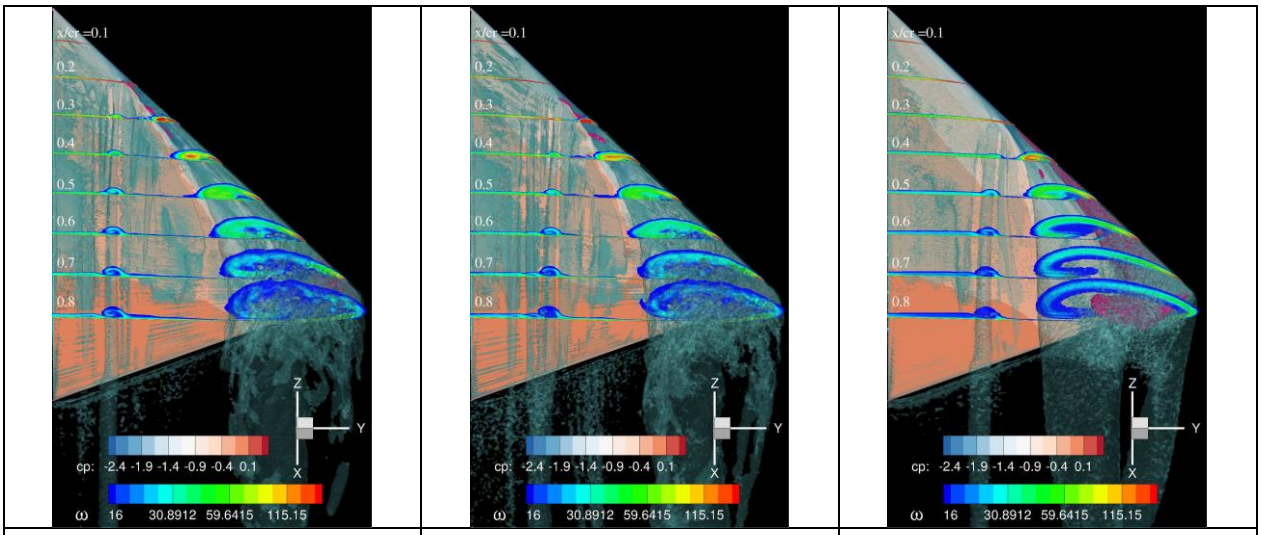

(a) RSM-DDES | (b) SA-RC-QCR-DDES | (c) RSM

Figure 36: Contours of the vorticity magnitude and iso-surface of λ_2 of the time-averaged flow field for the diamond wing.

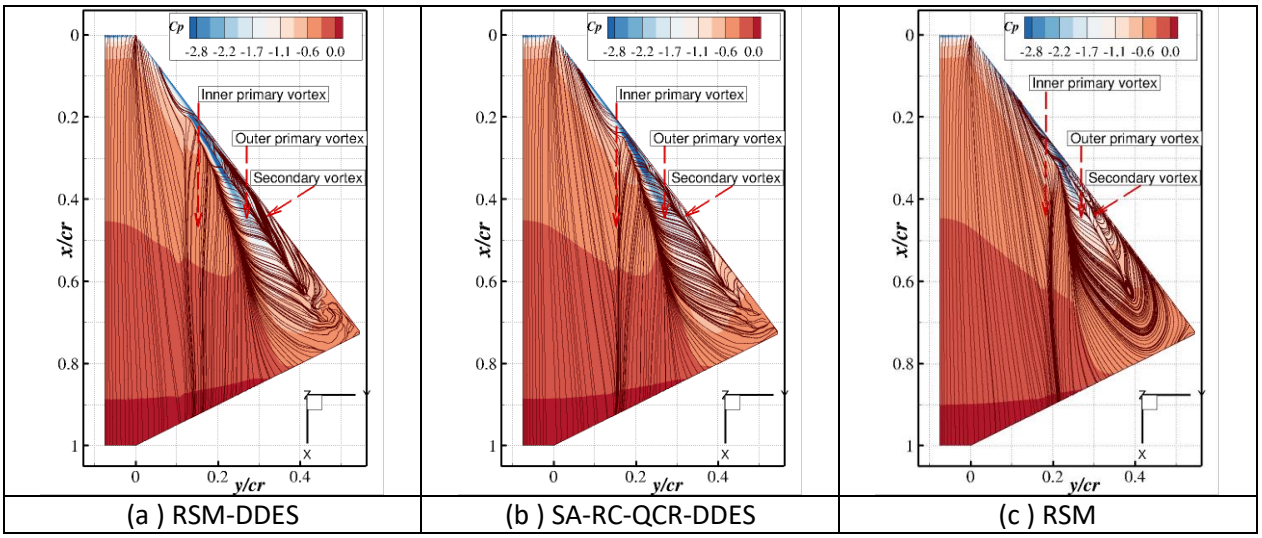

(a) RSM-DDES | (b) SA-RC-QCR-DDES | (c) RSM

Figure 37: Surface skin-friction lines and the contours of pressure coefficient.

The skin-friction lines along with the surface pressure distribution on the suction side of the wing are displayed in Figure 37. The skin-friction lines unveil the predicted inner primary and outer primary vortices by all the applied models. Additionally, there is also the evidence of a secondary vortex in all the predictions near the leading edge of the wing. In the DDES investigations based on RSM, a larger spanwise extend secondary vortex is predicted compared to SA-RC-QCR-based DDES. From the counters of cp on the surface, it is evident that the suction pressure associated with the outer primary vortex in RSM-DDES is almost the same as in SA-RC-QCR-DDES, indicating almost same vortex strength in the predictions.

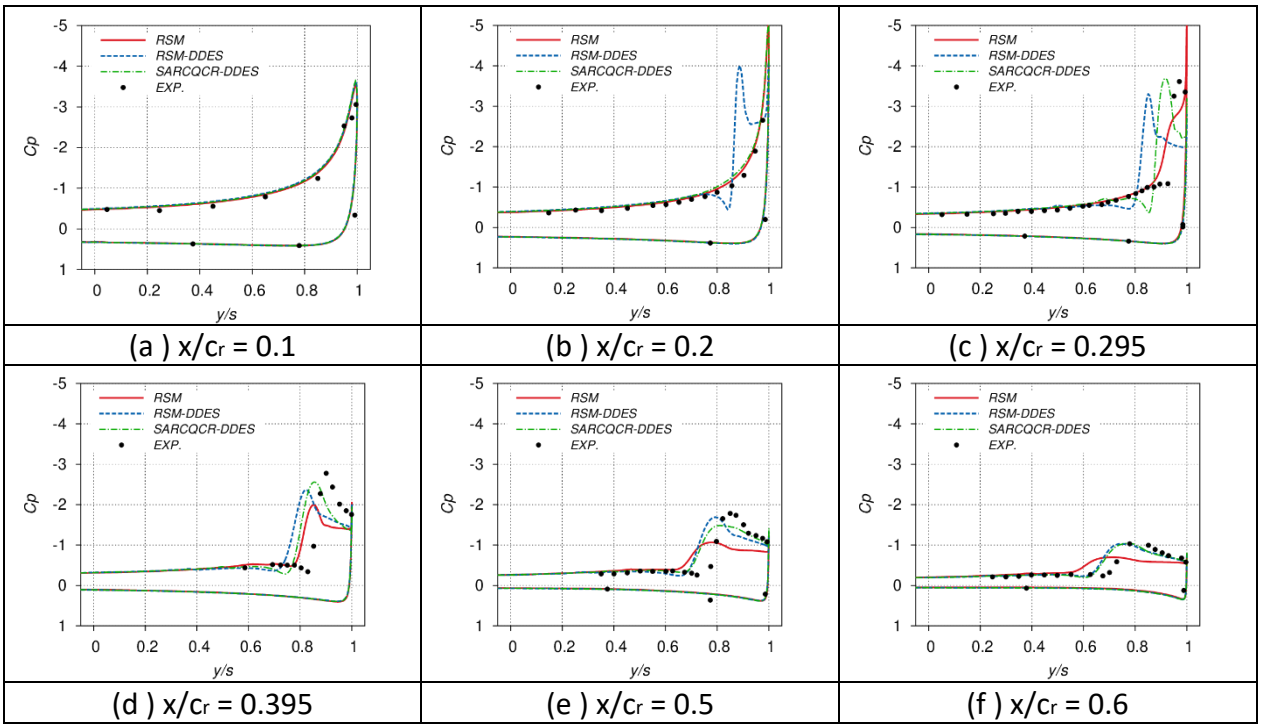

Figure 38: Cp distribution at different streamwise sections.

The comparison of the sectional pressure distribution is displayed in Figure 38. Here the RSM results are shown for reference. At the streamwise sections of $x/c_r = 0.1$ the RSM-DDES predicts attached flow. However, at $x/c_r = 0.2$, it predicts vortex separation as a result of the suction peak at the leading-edge collapses. At $x/c_r = 0.295$, in the experiments the inboard movement of the suction peak from the leading edge indicates flow separation and subsequent vortex formation. The location of the suction peak also indicates the vortex axis.

As can be seen in Figure 38 (c), all DDES predictions follows the experimental trend, however, the predicted vortex axis is more inboard compared to the experiments which is because of the earlier vortex separation than in the experiments.

In RSM-DDES, the vortex axis is located most inboard while in SA-RC-QCR the location is closer to the experiments. The reason for this trend is the flow separation which is predicted too far upstream in RSM-DDES while the SA-RC-QCR-DDES predicts the separation location closer to experimental data.

At $x/c_r = 0.395$, in the experiments a lower suction peak compared to the previous location is observed. This is because with the downstream distance the size of the vortex grows and its strength decreases. The location of cp_{min} indicates that the vortex core axis moves inboard with the downstream distance. At this streamwise station all the DDES predictions deliver the same cp level. At farther downstream locations almost the same level of cp peaks and the vortex core axis are predicted by all the DDES models.

Overall for this configuration, the DDES based on the RSM predicted too early separation as a result the subsequent vortex development is predicted poorly compared to the DDES based on SA-RC-QCR.

Discussion on RSM based DDES predictions

In the present work the RSM-DDES predicted earlier separation compared to RSM. The reason for earlier separation is most probably the blending function employed in the RSM-DDES computation. In the current investigation Menter's blending function F1 [12] is employed with which the RSM-DDES model switches from RANS to LES. Usually for RSM-DDES computations, Menter's blending function F2 [12] is employed. In the current investigation F1 is chosen to resolve the vortices which are located very close to the wall. Because of this, the RSM-DDES employed in the present work switches from RANS to LES within the attached boundary layer where the grid resolution is not fine enough and the flow too stable to quickly produce LES content. As a result lower total turbulent stresses within the boundary layer are predicted (so-called "modelled-stress depletion" [15]) which eventually lead to earlier flow separation in the RSM-DDES predictions than in RSM investigation.

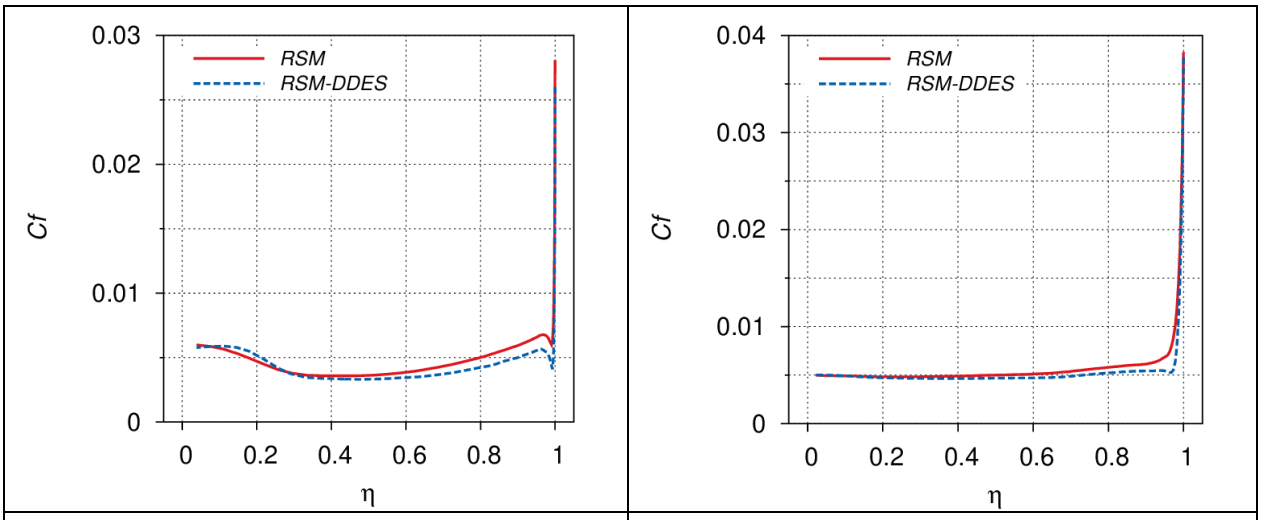

(a) Delta wing (b) Diamond wing

Figure 39: Cf along the wing span for delta and diamond wings

To demonstrate this, the cf along the wing span for the delta wing and diamond wing at x/c_r of 0.2 and 0.15, respectively, is shown in Figure 39. For both configurations, the cf is lower in RSM-

DDES than in RSM computations. The reason for this is the lower turbulence stresses in the boundary layer in RSM-DDES compared to RSM.

For future investigations, Menter's blending function F2 or the delay function f_d [16] used in SA-DDES are recommended, which are expected to improve the predictions of RSM-DDES for both configurations.

Summary and outlook

To evaluate the predictive capabilities of a Reynolds stress model (RSM) for separated vortex flows, investigations are carried out for the flow over a spheroid, a delta wing and a diamond wing. All the cases are characterized by separation from a smooth surface and subsequent vortex formation, the phenomena often observed on military configurations. Here the main objective is to explore the performance of RSM compared to eddy-viscosity models (EVM) and hybrid RANS/LES methods (HRLM) in the prediction of separated vortex flows. To this end, the aforementioned configurations are investigated using the SSG/LRR-ln(ω) Reynolds stress model and the predictions are compared to the predictions delivered by EVM and HRLM. In this work, the SA turbulence model coupled with the Rotation/Curvature correction and the Quadratic Constitutive Relation (QCR) are employed as to improve the predictions of the vortices and the normal Reynolds stress anisotropy which exists in the regions of secondary separation. For HRLM, the delayed detached eddy simulation based on SA and SA-RC-QCR are employed.

Prior to the performance studies, grid refinement and grid topology investigations are conducted. After observing grid independence of the predictions, performance studies using, first, RANS models, later HRLM based on EVM, and finally HRLM based on RSM are carried out on appropriate grids.

In the RANS performance study, investigations on the spheroid case unveiled that the predictions delivered by all the applied turbulence models are almost identical, that is, improvements in the predictions by applying RSM for this case are marginal compared to the other models. Comparing predictions with experiments show that the strength of the primary and secondary vortices still needs to be improved.

For the delta wing, the SA-RC-QCR predicted separation from the leading edge earlier than the one observed in the experiments. This led to an earlier formation of inner and outer primary vortices and an underprediction of the vortex strength and the associated pressure distribution compared to the experiments. In RSM the separation is predicted closer to the experimental separation from the leading edge which lead to improved predictions with respect to the pressure associated with the outer primary vortex. However, the strength of the inner primary vortex is underpredicted and its location is more inboard compared to experiments. For this case, still improvements with respect to inner primary vortex strength and location are required.

For the diamond wing, the SA-RC-QCR predicted separation from the leading edge earlier than in the experiments, however, the downstream development of the outer primary vortex is in good agreement with the experiments with regard to the pressure associated with the vortex and its location. In the RSM predictions, vortex separation from leading edge is observed a bit downstream of experimental separation location. Additionally, the primary vortex is enlarged and the pressure associated with it is overpredicted. Among the applied models, the SA-RC-QCR delivered improved predictions.

For the evaluation of hybrid RANS/LES, investigations are carried out with the SA-DDES and SA-RC-QCR-DDES for the delta and diamond wing. For both configurations, the SA-RC-QCR-DDES predicted separation too early and delivered weaker vortices and located more inboard on the wing compared to the experiments. However, the SA-DDES predicted vortex separation close to experiments. In the case of delta wing, the SA-DDES predicted inner and outer primary vortices, but after a short downstream distance merging of the inner primary vortex with the outer primary vortex is observed. The trend delivered in the SA-DDES is different from the experiments. For the diamond wing, both inner and outer primary vortices are predicted and the pressure associated with the outer primary vortex observed to be in good agreement with the experiments. Comparison of RSM and HRLM for the aforementioned configurations unveils that the RSM predicts the flow better than HRLM for delta wing while for Diamond wing, SA-DDES represents the flow better than RSM.

Finally, RSM-based DDES is employed to investigate the flow over the delta wing and the diamond wing in order to explore the potential of the combination of both methods. For both configurations, RSM-DDES performed poorly by predicting too upstream vortex separation and weaker inner and outer primary vortices. It was found, however, that an unsuitable “shielding” function applied in these RSM-DDES computations may have caused modelled-stress depletion in the early boundary layer and, thus, the premature separation.

In spite of some degree of agreement between RSM predictions and experiments, still improvements in the predictions are required with regard to the strength and location of the inner primary and outer primary vortices.

Dissemination

The following papers are foreseen as the DLR institute reports in 2022.

- RANS investigations of vortex separated flows by V. Togiti, A. Krumbein
- Scale-resolving simulation of vortex separated flows by V. Togiti, A. Krumbein and A. Probst

References

[1] N. Frink, M. Tomac and A. and Rizzi, "Collaborative study of incipient separation on 53° swept diamond wing," *Aerospace Science and Technology,* vol. 57, pp. 76-89, 2016.

[2] M. Ghoreyshi, K. Ryszka, R. Cummings and A. Lofthouse, "Vortical flow prediction of a diamond wing with rounded leading edges," *AerospaceScienceandTechnology,* pp. vol. 57, pp. 103-117, 2016.

[3] S. Braun, U. A., B. Eisfeld and E. Stumpf, "Numerical Simulation of Vortex Roll-Up Processes Using the SSG/LRR-w," *New Results in Numerical and Experimental Fluid Mechanics X Notes on Numerical Fluid Mechanics and Multidisciplinary Design ,* vol. 132, pp. 481-491, 2016.

[4] V. Togiti, V. Ciobaca, B. Eisfeld and T. Knopp, "Numerical simulation of steady blowing active flow control using a differential reynolds stress model," in *CEAS/KATnet II*, Bremen, Germany, 2009.

[5] T. G. Wetzel, R. L. Simpson and C. J. Chesnakas, "Measurement of three-dimensional crossflow separation," *AIAA Journal,* pp. vol. 36(4), pp. 557-568, 1998.

[6] D. Hummel and G. Redeker, "A new vortex flow experiment for computer code validation," in *RTO-AVT Symposium on Vortex Flow and High Angle of Attack*, Loen, Norway, 7–11 May, 2001.

[7] J. Luckring and D. Hummel, "What was learned from the new VFE-2 experiments," *Aerosp. Sci. Technol.,* vol. 24, no. 1, p. 77–88, 2013.

[8] A. Hövelmann, M. Grawunder, A. Buzica and C. Breitsamter, "AVT-183 diamond wing flow field characteristics Part 2: Experimental analysis of leading-edge vortex formation and progression," *Aerospace Science and Technology,* vol. 57, p. 31–42, 2016.

[9] M. L. Shur, M. K. Strelets, A. K. Travin and P. R. Spalart, "Turbulence Modeling in Rotating and Curved Channels: Assessing the Spalart-Shur Correction," *AIAA journal,* pp. Vol. 38, No. 5, pp. 784-792, 2000.

[10] M. Mani, D. A. Babcock, C. M. Winkler and P. R. and Spalart, "Predictions of a Supersonic Turbulent Flow in a Square Duct," in *AIAA Paper 2013-0860*, 2013.

[11] P. R. Spalart and S. R. Allmaras, " A One-Equation Turbulence Model for Aerodynamic Flows," in *Recherche Aerospatiale*, 1994.

[12] F. R. Menter, "Two-Equation Eddy-Viscosity Turbulence Models for Engineering Applications," *AIAA Journal,* pp. Vol. 32, No. 8, pp. 1598-1605, 1994.

[13] B. Eisfeld, C. Rumsey and V. Togiti, "Verification and Validation of a Second-Moment-Closure Model," *AIAA Journal,* Vols. Vol. 54, No. 5, pp. pp. 1524-1541, 2016.

[14] S. Braun, "Implementation of a ln(w) based SSG/LRR Reynolds Stress Model into the DLR-TAU Code," Institutsbericht, DLR-IB-AS-BS-2019-37, Report of the Institute of Aerodynamics and Flow Technology, Braunschweig, 2019.

[15] P. Spalart, S. Deck, M. Shur, K. Squires, M. K. Strelets and A. Travin, "A New Version of Detached-Eddy Simulation, Resistant to Ambiguous Grid Densities," *Theoretical and Computational Fluid Dynamic,* Vols. 0935-4964, pp. 181-195, July 2006..

[16] M. Gritskevich, A. Garbaruk, J. Schütze and F. Menter, "Development of DDES and IDDES Formulations for the k-ω Shear Stress Transport Model," *Flow Turbulence and Combustion ,* vol. 88, no. 3, p. 431–449, 2012.

[17] A. Probst, R. Radespiel and K. T., "Detached-Eddy Simulation of Aerodynamic Flow Using a Reynolds Stress Background Model and Algebraic RANS/LES Sensor," in *AIAA Paper No. 3206*, 2011.

[18] D. Schwamborn, T. Gerhold and R. Heinrich, "The DLR TAU-Code: Recent Applications in Research and industry," in *Europen Conference on CFD, ECCOMAS CFD*, 2006.

[19] A. Probst, J. Lowe, S. Reuß, T. Knopp and R. Kessler, "Scale-Resolving Simulations with a Low-Dissipation Low-Dispersion Second-Order Scheme for Unstructured Flow Solvers," *AIAA Journal,* vol. 54, no. 10, p. 2972–2987, 2016.